主論文1

Sea Surface Dynamic Topography Fluctuations Southeast of Japan Estimated from Geosat altimetry data

Kaoru Ichikawa

Department of Civil and Ocean Engineering, Faculty of Engineering, Ehime University, Matsuyama, Ehime 790, Japan

Shiro Imawaki

Research Institute for Applied Mechanics, Kyushu University, Kasuga, Fukuoka 816, Japan

Short title: SSDT FLUCTUATIONS AS SEEN BY GEOSAT

Abstract. Optimal interpolation method is applied to Geosat altimetry data both to remove orbit error and to separate temporal mean sea surface dynamic topography (SSDT) from temporal fluctuations around the mean. The fluctuation SSDT is quantitatively evaluated by sea level data from eight tide gauge stations at Japanese islands. The correlation coefficient of the two sea-level variations is 0.49. It increases to 0.85 when unfavorable stations for evaluating the fluctuation SSDT are excluded and when seasonal variations of the areal averages lost in the present optimal interpolation are taken into account. Improvement of the geoid model by combined use of Seasat altimetry data and hydrographic data is also validated. In a local area where *in situ* hydrographic observations during the Seasat mission exist, the geoid model has been significantly improved so that the absolute SSDT can be determined from combination of the altimetry data and the geoid model; the absolute SSDT describes the onset event of the quasi-stationary large meander of the Kuroshio south of Japan very well. Out of this local area, however, errors of magnitudes of several tens of centimeters still remain in the improved geoid model.

1. Introduction

There would be no doubt that satellite altimetry is one of the most fruitful measurement techniques in physical oceanography, but some special procedures are still required for its usage. One of these procedures is the radial orbit error reduction. The sea surface height (hereinafter abbreviated as SSH) observed by a satellite altimetry system consists of two distance determinations; distance between the satellite and the sea surface at nadir is measured by the altimeter, while height of the satellite is independently calculated. Owing to the refinement of the gravitational field models and to the progress in satellite tracking systems, determination of the latter has been improved so that its error (radial orbit error) has decreased from a few meters to several tens of centimeters, or even several centimeters for higher-altitude TOPEX/POSEIDON satellite (Koblinsky *et al.*, 1992; Wagner and Tai, 1994). Uncertainty of several tens of centimeters is, however, still similar to or larger than the magnitude of expected oceanic signals. Because the temporally variant part of this error is known to have a spectrum peak at a frequency once per satellite revolution around the Earth (*e.g.* Lerch *et al.*, 1982), it is usually removed from SSH data as a long-wavelength component along a subsatellite track. One should notice, however, that this procedure also removes oceanic signals of long wavelengths no matter how small the magnitude of the radial orbit error becomes.

Another special procedure is required to separate the temporal mean from temporal fluctuations around the mean. The SSH observed by the altimetry system is further converted to the sea surface dynamic topography (hereinafter abbreviated as SSDT) by removing both equi-geopotential heights near the sea surface (or geoid heights) and sea-surface height variations (*e.g.* tides) whose frequencies are higher than the Coriolis parameter; it is this SSDT that is directly related to the geostrophic velocity field at the sea surface. The geoid models have been improved year by year, but they still have errors larger than expected oceanic signals, except for models in some local regions

(Rapp and Wang, 1994) and models of very large scales (Nereme *et al.*, 1990). Since the geoid can be considered as temporally invariant, the error in the geoid models remains only in the temporal mean and hence the fluctuation part of SSDT can be determined free from the geoid error contamination. In order to separate the temporal mean from the fluctuations, so-called collinear method is widely used (*e.g.* Cheney *et al.*, 1983); this method based on the assumption that SSH at a given position is repeatedly observed by an altimeter so that the temporal mean is simply calculated by averaging each SSH after the radial orbit errors are removed individually. This method is handy and accurate as far as the altimetry observations are performed at exactly the same positions, but obviously it can not be applied to altimetry data which do not follow exactly repeating orbits, such as some periods of Seasat and ERS (European Remote Sensing satellite)–1 observations.

More satellites carrying altimeters are expected to be launched in the near future, but there is no guarantee that their orbit calculations are accurate enough nor that all of them will take exactly repeating orbits. Therefore, we should construct an accurate and robust method which can consistently handle any altimetry data sets of different accuracies and data sampling patterns. Use of the optimal interpolation is one of the candidates satisfying the required conditions. The optimal interpolation produces statistically least-squared-error linear estimates at arbitrary positions and their estimated errors from noisy input data, provided that the covariance functions of the signal and noise are known in advance (Bretherton *et al.*, 1976). The method is widely used to produce maps of the fluctuation part of SSDT from irregularly distributed along-track altimetry observations after the radial orbit errors are removed by the conventional methods, but it can also be applied both to orbit error removal (Wunsch and Zlotnicki, 1984; Mazzega and Houry, 1989) and to the temporal mean separation from the fluctuations (Ichikawa and Imawaki, 1992). Although the number of the data points is practically limited in this method since it requires fairly big computer

to process, the method permits us to treat non-exactly-repeating altimetry data and to remove orbit errors accurately by utilizing knowledge of the magnitude of the radial orbit errors.

Another strategy for the use of altimetry data in the near future is to improve the present geoid model by the combined use of the altimetry data and other hydrographic observations. As explained above, the temporal mean SSDT determined from the altimetry data is contaminated by the error in the geoid model. On the other hand, this also guarantees that if we can obtain the true SSDT through any other method, the geoid error can be determined as the discrepancy between the true SSDT and the altimetric SSDT so that the geoid model used in the analysis can be improved (Glenn *et al.*, 1991; Imawaki *et al.*, 1991). Once the present geoid model is improved with the altimetry data by this method, it can be applied to any future altimetry data set to produce absolute SSDT without contamination of the geoid error. However, none has yet been applied the geoid model improved through this method to the other altimetry data set to produce the absolute SSDT.

Altimetry data in an area southeast of Japan have been successfully analyzed by the use of optimal interpolation. The method was applied to Seasat altimetry data and both the temporal mean elevation field during the Seasat three-month period and the fluctuation part of SSDT were accurately determined (Imawaki *et al.*, 1991; Ichikawa and Imawaki, 1992). The estimated temporal mean elevation filed was further used to estimate the geoid error with the aid of an approximated mean SSDT field determined by hydrographic observations (Imawaki *et al.*, 1991). This approximated mean SSDT was also combined with the fluctuation SSDT to produce an approximated absolute SSDT, or composite SSDT, which was revealed to be useful to describe variations of oceanic conditions in the study area very well.

In the present paper, we extend the method as to treat a large number of data, and apply it to one-year long Geosat altimetry data southeast of Japan accord with the

above-mentioned improved geoid model, in order to accurately determine the temporal mean elevation field and the fluctuation part of SSDT during the Geosat study period. One of the objectives of the present paper is to investigate the improvement of the geoid model through combined use of Seasat altimetry data and hydrographic observations; this will be performed by evaluating the estimated temporal mean elevation field during the Geosat period from the viewpoint whether the field is depart from the expected mean SSDT because of the contamination of large geoid error. The other objective is to quantitatively evaluate the optimal interpolation method; the estimated fluctuation SSDT is evaluated by tide gauge records at Japanese islands. The composite SSDT during the Geosat period is also determined from the estimated fluctuation SSDT, and is shown to describe variations of the Kuroshio and the Kuroshio Extension, and rings separated from them vividly, which is described in a separated paper (Ichikawa and Imawaki, 1994). The method we used is explained in Section 2 and its performances are studied in Section 3. The data used in the present analysis is described in Section 4, while the results are described in Section 5, and discussed in Section 6. Finally, concluding remarks are summarized in Section 7.

2. Method

The instantaneous sea surface height $S(\mathbf{r},t)$ observed by an altimeter at time t can be written as

$$S(\mathbf{r},t) = \zeta(\mathbf{r},t) + \{N(\mathbf{r}) + \varepsilon_N(\mathbf{r})\} + \{\varepsilon_s(\mathbf{r}) + \varepsilon_r(t)\} + \varepsilon_m(t), \tag{1}$$

where $\mathbf{r}$ is the horizontal position vector of the observation point on the sea surface, $\zeta(\mathbf{r},t)$ is the SSDT, $N(\mathbf{r})$ is the geoid height in the best available model which has an unknown error $\varepsilon_N(\mathbf{r})$, $\varepsilon_s(\mathbf{r}) + \varepsilon_r(t)$ are the systematic and random orbit errors, and $\varepsilon_m(t)$ is the random measurement error. Here it is understood that $S(\mathbf{r},t)$ has been corrected for distance measurement errors (several path length corrections) and that

high frequency fluctuations have been eliminated (*e.g.* tide corrections); the errors of all these corrections as well as the altimeter sensor error are included in the random measurement error $\varepsilon_m(t)$. As explained in the previous section, we need to separate the instantaneous SSDT $\zeta(\mathbf{r},t)$ into the temporal mean SSDT $\overline{\zeta}(\mathbf{r})$ over the entire period and the deviation $\zeta'(\mathbf{r},t)$ from the mean, or $\zeta(\mathbf{r},t) = \overline{\zeta}(\mathbf{r}) + \zeta'(\mathbf{r},t)$. Equation (1) is then rewritten as

$$R(\mathbf{r},t) = H(\mathbf{r}) + E(\mathbf{r},t), \tag{2}$$

where

$$\begin{aligned} R(\mathbf{r},t) &= S(\mathbf{r},t) - N(\mathbf{r}), \\ H(\mathbf{r}) &= \overline{\zeta}(\mathbf{r}) + \varepsilon_N(\mathbf{r}) + \varepsilon_s(\mathbf{r}), \\ E(\mathbf{r},t) &= \zeta'(\mathbf{r},t) + \varepsilon_r(t) + \varepsilon_m(t), \end{aligned}$$

Here the errors of random nature, $\varepsilon_r(t)$ and $\varepsilon_m(t)$, are assumed to be negligible when they are averaged. Regarding $H(\mathbf{r})$ as the signal and $E(\mathbf{r},t)$ as the noise of the instantaneous observation $R(\mathbf{r},t)$, the mean elevation $H(\mathbf{x})$ at an arbitrary position $\mathbf{x}$ can be estimated by the optimal interpolation from the entire input data set $\{R(\mathbf{r},t)\}_{\forall_t}$ (where the formula $\{R\}_{\forall_t}$ denotes the ensemble of R for all t). Practically, however, the method can not be applied directly to a large number of input data because it needs to operate a matrix of (number of data points)×(number of data points) elements. In order to relax this computational limitation, we further divide the entire period into several subperiods since the coverage of the altimetry measurements is generally repeated. The instantaneous SSDT $\zeta(\mathbf{x},t_q)$ at an arbitrary position $\mathbf{x}$ and time t_q which belongs to a subperiod q is now separated into the mean SSDT over the given subperiod q, or $\overline{\zeta}(\mathbf{x}) + \zeta'_q(\mathbf{x})$, and the departure $\zeta''_q(\mathbf{x},t_q)$ from it. Here, $\zeta'_q(\mathbf{x})$ is equivalent to the temporal mean of the deviation SSDT $\zeta'(\mathbf{x})$ over the subperiod q. Then Eq. (2) at an

arbitrary observation time t_q in the subperiod q can be rewritten as

$$R(\mathbf{r}, t_q) = H_q(\mathbf{r}) + E_q(\mathbf{r}, t_q), \tag{3}$$

where

$$\begin{aligned} R(\mathbf{r}, t_q) &= S(\mathbf{r}, t_q) - N(\mathbf{r}), \\ H_q(\mathbf{r}) &= \overline{\zeta}(\mathbf{r}) + \zeta'_q(\mathbf{r}) + \varepsilon_N(\mathbf{r}) + \varepsilon_s(\mathbf{r}), \\ E_q(\mathbf{r}, t_q) &= \zeta''_q(\mathbf{r}, t_q) + \varepsilon_r(t_q) + \varepsilon_m(t_q). \end{aligned}$$

Since the duration of the subperiod q are chosen to satisfy the computational limitation, we can now estimate the mean elevation $H_q(\mathbf{x})$ over the given subperiod q by the optimal interpolation from the input data set $\{R(\mathbf{r}, t_q)\}_{\forall t_q}$ during the subperiod q. Note that the data coverage in each subperiod $\{R(\mathbf{r}, t_q)\}_{\forall t_q}$ may be similar, but is not necessarily exactly the same. Denoting the duration of a subperiod q as T_q, the mean elevation $H(\mathbf{x})$ over the entire period would be estimated simply by the weighted mean

$$H(\mathbf{x}) = \frac{\sum_q T_q H_q(\mathbf{x})/\epsilon_q(\mathbf{x})}{\sum_q T_q/\epsilon_q(\mathbf{x})}, \tag{4}$$

where $\epsilon_q(\mathbf{x})$ is the estimated error of $H_q(\mathbf{x})$ which is provided by the optimal interpolation.

With the estimated mean elevation $H(\mathbf{x})$ over the entire period, Eq. (2) for an arbitrary observation time t_p in a subperiod p can be further transformed as

$$R'(\mathbf{r}, t_p) = H'_p(\mathbf{r}) + E'_p(\mathbf{r}, t_p), \tag{5}$$

where

$$\begin{aligned} R'(\mathbf{r}, t_p) &= S(\mathbf{r}, t_p) - N(\mathbf{r}) - H(\mathbf{r}), \\ H'_p(\mathbf{r}) &= \zeta'_p(\mathbf{r}), \\ E'_p(\mathbf{r}, t_p) &= \zeta''_p(\mathbf{r}, t_p) + \varepsilon_r(t_p) + \varepsilon_m(t_p). \end{aligned}$$

Now we can estimate the time invariant component $H'_p(\mathbf{x})$ during the subperiod p using the optimal interpolation regarding the data set $\{R'(\mathbf{r}, t_p)\}_{\forall t_p}$ as the input data and $E'(\mathbf{r}, t_p)$ as their noise. Note that the time invariant component $H'_p(\mathbf{x})$ consists only of the subperiod-mean deviation SSDT $\zeta'_p(\mathbf{x})$ from the entire-period-mean SSDT $\overline{\zeta}(\mathbf{x})$. Provided that the duration of the subperiod p is sufficiently short, the component $\zeta'_p(\mathbf{x})$ would represent the quasi-instantaneous temporal fluctuations of SSDT and hence is called hereinafter the fluctuation SSDT. One would notice that durations of the subperiods in Eq. (3) and ones in Eq. (5) are not necessarily to be the same. In general, the subperiod duration T_q in Eq. (3) should be long to increase spatial resolution of the mean elevation field $H_q(\mathbf{x})$ over the subperiod, whereas those in Eq. (5) should be short to increase temporal resolution of the fluctuation SSDT as far as the observation point distribution is not sparse. An exception is the case when the data are in an exactly repeating mission, in which the observation point distribution cannot be denser once the duration of the subperiod T_q exceeds the exact repeating cycle (*e.g.* 17 days for Geosat).

Covariance functions of both the signal and noise must be given in advance in the optimal interpolation. In practice, however, it is too difficult to generalize these covariances since they have complicated anisotropic and inhomegeneous characters. Therefore, in the present analysis, we decided to use simple functions to represent those covariances rather than complicated statistical functions. For the covariance function of the signal, we chose the negative squared exponential, or the Gaussian shape spatial function, which is widely used to represent aperiodic fields in the atmospheric sciences (Thiébaux and Pedder, 1987); the spatial covariance function $W(|\mathbf{s}|)$ of the signal is given by

$$W(|\mathbf{s}|) = {w_0}^2 \exp\left[-(|\mathbf{s}|/L)^2\right], \tag{6}$$

where $|\mathbf{s}|$ is horizontal distance between two positions on the sea surface, L the spatial decorrelation length scale of the field, and w_0 the magnitude of the signal. Note that we need not to consider the time dependency of the covariance function since the signal is

chosen to be temporally invariant both in Eqs. (3) and (5).

Use of Gaussian shape covariance function, however, may induce two possible problems: One is that the data distant from an estimation point $\mathbf{x}$ with respect to the decorrelation scale L are not utilized in reconstruction of the signal, no matter how strongly they correlate with it. The other is that the Gaussian shape covariance function can not correctly handle the data with negative correlations to the signal; this would be serious especially when the data close to the estimation point with respect to L have negative correlations (Thiébaux and Pedder, 1987). Therefore, the choice of the decorrelation scale L is a compromise of these two possible problems. In other words, L should be determined to maximize the index $Q(\mathbf{x})$ of correct data utilization in reconstruction of the signal at position $\mathbf{x}$, which can be expressed as

$$Q(\mathbf{x}) = \sum_{i=1}^{N} \frac{C(\mathbf{s}_i;\mathbf{x})W(|\mathbf{s}_i|)}{C(\mathbf{0};\mathbf{x})W(0)} \tag{7}$$

where $C(\mathbf{s};\mathbf{x})$ is the unknown true covariance at the point $\mathbf{x}$, $\mathbf{s}_i = \mathbf{r}_i - \mathbf{x}$ the horizontal position vector of i-th observation point $\mathbf{r}_i$ with respect to $\mathbf{x}$, and N the number of the observations. However, since it is practically impossible to determine $C(\mathbf{s};\mathbf{x})$ for all points $\mathbf{x}$, smaller L would be secure to avoid negative $Q(\mathbf{x})$ at any $\mathbf{x}$, although we may loose large contribution from distant data points for some $\mathbf{x}$. Therefore, we choose as small L as possible as long as several data points can be referred in the reconstructing the signal; we set L as 150 km, 1.5 times the distance between adjacent tracks. In addition, we decide not to use the estimated signals in data-sparse areas where the estimates strongly depend on the choice of covariance functions (Thiébaux and Pedder, 1987).

The noise covariance function $\phi(\Delta t)$ is here given by

$$\phi(\Delta t) = {\sigma_0}^2\ \delta(\Delta t) + {\sigma_1}^2\ \exp\left[-(\Delta t)^2/T_1^2\right]\ \cos\left[2\pi(\Delta t)/T_0\right], \tag{8}$$

where the first term comes from the random measurement error $\varepsilon_m(t)$ of the altimeter as well as from the deviation SSDT $\zeta_p''(\mathbf{r},t)$ and the second term comes from the random

radial orbit error $\varepsilon_r(t)$ (Wunsch, 1986; Wunsch and Zlotnicki, 1984). Here σ_0 represents the magnitude of the measurement error at a data point, δ the Dirac-delta, σ_1 the rms (root-mean-squared) amplitude of the random radial orbit error, Δt the time difference between two observations, T_0 the period of the dominant component of the random radial orbit error (namely the revolution period of the satellite orbit) and T_1 the decorrelation time scale for the random radial orbit error, which is related to the band-width of the frequency peak of the dominant component of the orbit error.

The parameters of signal and noise covariance functions (6) and (8) are chosen empirically as follows. For the covariance function of the noise, $\sigma_0 = 0.2$ m, $\sigma_1 = 1$ m, $T_0 = 6041$ s (100.7 min), and $T_1 = 20T_0$ (see Lerch *et al.*, 1982; Tapley *et al.*, 1982; Wunsch and Zlotnicki, 1984; Haines *et al.*, 1990). For the covariance function of the mean elevation field in Eq. (3), w_0 is 0.4 m , whereas for that of the fluctuation SSDT field in Eq. (5), w_0 is 0.2 m. As noted above, we did not use the estimated values when the estimated error $\epsilon_q(\mathbf{x})$ exceeds 0.3 m in Eq. (3) or $\epsilon_p(\mathbf{x})$ exceeds 0.16 m in Eq. (5) in order to exclude the data-sparse area.

3. Optimal Interpolation Tests

In order to understand the performance of the covariance functions used in the present analysis, we made test analyses for artificial observation data and compared the estimated field with the known true field. We first produce artificial observation data from a given true field by extracting its values at simulated altimetry data points and by adding artificial noises, and then the field is reconstructed by the optimal interpolation from those artificial observation data, and finally it is evaluated by comparing with the known true field. For the convenience of the following discussions, we first focus on the Gaussian shape signal covariance function (6) and the Dirac-delta noise covariance function as the first term of function (8). Then the performance of the orbit error noise covariance function as the second term of function (8) is considered later.

For the test of the Gaussian shape signal covariance and the Dirac-delta noise covariance functions, an artificial altimetry observation at a point $\mathbf{r} = (x, y)$ and time t is given by the formula

$$\sum_{i=1}^{N} \alpha_i \cos 2\pi(x/(L_x)_i + \theta) \cos 2\pi(y/(L_y)_i + \theta') + \beta R(t), \tag{9}$$

in which the first term represents the true field and the second the noise; N is the number of wave components, α_i the amplitude of i-th wave component, $(L_x)_i$ and $(L_y)_i$ the wavelengths for x and y directions for i-th wave component, respectively, θ and θ' arbitrary phase constants, $R(t)$ the normalized random number function, and β the strength of the noise. Then the true field is reconstructed from the artificial data set following the same procedures used in the present paper (see Sections 2 and 4); namely, 10 data points along tracks are averaged and the height field is estimated by the optimal interpolation using the Gaussian shape covariance function with $L = 150$ km for the signal covariance and the Dirac-delta function for the noise covariance. An example is shown in Fig. 1. We made several tests for different combinations of N, L_x, L_y, α and β including L_x or L_y $=\infty$ cases, and parameters w_0 and σ_0 of the optimal interpolation. Fig. 1

For variations of N, L_x, and L_y, the results are summarized in Fig. 2. The larger the the scale of the true field is, rms difference between the true field and the reconstructed field is small, namely the accurate reconstruction by the optimal interpolation. When the wavelength L_x or L_y becomes less than approximately $2L$ (300 km), however, the field can not be reconstructed correctly; the estimated field results in psudo structures having wavelengths different from those of the true field. This is somewhat reasonable since the length of a packet of positive or negative values in the true field (see Fig. 1(a)) is shorter than the decorrelation length scale L for these cases; note that the index $Q(\mathbf{x})$ in Eq. (7) would be negative for structures whose L_x or L_y is shorter than $2L$. Although the rms height of such deformed structures are reduced from that of the true field as indicated by crosses in Fig. 2, it is concluded that small-scale structures of Fig. 2

strong magnitude should be excluded from the signal to be reconstructed. This result leads to a technical suggestion; when intense small-scale structures are known to be included in the signal such as mean SSDT $\overline{\zeta}(\mathbf{r})$ variations associated with the Kuroshio and the Kuroshio Extension, in Eq. (3), some pre- and post-processes are necessary to protect them to be lost or deformed through the optimal interpolation. Namely, an approximation of those structures should be removed from the input data as a "first guess" before the optimal interpolation and is then added back to the estimated field after the interpolation. In the present analysis, we used climatological mean SSDT as an approximation of the signal $H_q(\mathbf{x})$ in Eq. (3); therefore it is the deviation from the approximation to be interpolated with the Gaussian shape covariance function, rather than the mean elevation field itself. Note that the results hold for fields composed by several waves ($N \geq 2$), and therefore they would be adopted to arbitrary shapes of the input field taking the Fourier decomposition into account.

Figure 3 summarize the results of various combinations of α, β, w_0 and σ_0. In the figure, rms difference between the true field and the reconstructed field are plotted against various combinations of parameters w_0 and σ_0 used in the optimal interpolation; these calculations are conducted for two input data sets with same signal strength $\alpha =$ 0.2 m but different noise magnitudes of $\beta = 0.02$ m (solid line) and $\beta = 0.2$ m (dotted line). In general, as the signal-to-noise (SN) ratio given in the optimal interpolation (w_0/σ_0) decreases, the estimated field becomes smoother in order to exclude noises in the observation data by smoothing. On the contrary, when too high SN ratio are provided in the optimal interpolation, the estimated field becomes very rough by inclusion of noises due to overconfidence of the input data. As a result, most accurate reconstruction of the field is expected when the ratio w_0/σ_0 is chosen close to the true SN ratio of the input data (indicated by triangles in Fig. 3). Errors in reconstruction of the field induced by invalid choices of w_0/σ_0 ratio, however, do not seem to be very severe, as far as the order of the ratio is the same as the true SN ratio.

Fig. 3

In order to study the performance of the radial orbit error removal, we made another set of tests which includes artificial orbit errors. For this series of tests, the sea surface height observation at a point $\mathbf{r}$ and time t is given by

$$\begin{aligned} A(x-x_c) &+ B(y-y_c)+C \\ &+ \beta R(t)+\gamma/\sqrt{1+2d\exp(-1)}\,\{\cos(\omega t+\theta) \\ &+ d\exp(-1)\,[\cos((\omega+\Delta\omega)t+\theta')+\cos((\omega-\Delta\omega)t+\theta'')]\} \end{aligned} \tag{10}$$

in which the first three terms represents the true field and the rest terms the noise; A and B are tilts of the true field plane in x and y directions, respectively, C the areal averaged height over the study area, $(x_c,\ y_c)$ the central point of the study area, β the amplitude of random noise, $R(t)$ the normalized random number function, γ the magnitude of the radial orbit error, ω the frequency of the orbit revolution, $\Delta\omega$ the band-width of the frequency peak of the random orbit error, d the switching parameter (0 or 1), and all θ, θ' and θ'' are arbitrary phase constants. The last term in Eq. (10) represents the radial orbit error of dominant frequency ω with $\Delta\omega$ band-width when $d=1$. We set $\gamma=1$ m, $\omega=2\pi/\tilde{T}_0$ ($\tilde{T}_0=6003$ s as the revolution cycle of the simulated orbit), $\Delta\omega=0.04\omega$, and $\beta=0.2$ m for several combinations of A, B, C and d, and reconstruct the fields by the optimal interpolation with the signal covariance function (6) and the noise covariance function (8) using parameters of $w_0=0.2$ m, $L=150$ km, $\sigma_0=0.2$ m, $\sigma_1=1$ m, $T_0=\tilde{T}_0$, and $T_1=20T_0$. The results indicates that no matter how we choose d, A and B, the field can be reconstructed correctly with slight distortion. For any choice of C, however, the areal average of the study field ($16°\times 16°$) is always lost in the estimated field; the areal average is considered to be removed as a part of the radial orbit error. Note that when the conventional simple radial orbit error reduction procedure is applied, the reconstructed field would become a zero field since the procedure removes all tilt and bias structures along subsatellite tracks, no matter which is the true field signal or the orbit error.

From the results of all those tests, oceanic signals having wavelengths larger than twice the decorrelation length scale L are expected to be accurately reconstructed from altimetry data by the present optimal interpolation except the spatial averaged height over the domain, provided that SN ratio given in the analysis is of the same order with the true ratio. In addition, when the input data are known to include significant small-scale oceanic signals, additional pre- and post-processing are required. Namely, an approximation field should be removed from the input data before the optimal interpolation and be added back to the estimated field after the interpolation; this is the case for the signals in Eq. (3).

4. Data

We used Geosat altimetry data for the area southeast of Japan (20°– 45°N, 120°–150°E) during the first year of the Exact Repeat Mission (ERM) (from November 8, 1986, to November 17, 1987). We did not use the data in the second and third years of the ERM since the data distribution in the study area during such period was too sparse compared with that of the first year. Geosat altimetry data used in the present analysis were distributed as Geophysical Data Records (GDR) by the National Oceanic and Atmospheric Administration (NOAA) (Cheney *et al.*, 1987). Separately distributed orbit height data were also used (Haines *et al.*, 1990). After correcting measurement errors supplied or suggested in GDR (ionospheric free-electron, tropospheric dry-air and tropospheric water vapor, solid and Schwiderski's ocean tides and EM bias corrections) and carefully excluding extreme or doubtful data which were judged by eye, we averaged the data over 10 data points along tracks (67 km) to reduce measurement errors and small-scale fluctuations as well as the total amount of data. Here, marginal seas such as the Japan Sea, the Yellow Sea, the Okhotsk Sea and part of the East China Sea were excluded because ocean tide corrections are known inaccurate in those areas. The number of data points after 10-point averaging in each cycle is shown in Table 1 Tab. 1

together with the start and end dates. An example of data point distribution in the present selected area is shown in Fig. 4 for the cycle of densest data coverage (Cycle 2). Distances between adjacent tracks are approximately 100 km at these latitudes, and data points are almost uniformly distributed. Fig. 4

The geoid model used here was originally obtained from marine gravity data (Ganeko, 1983) and improved by Seasat altimetry data combined with the sea surface geopotential anomaly data (Imawaki *et al.*, 1991). We also used climatological mean SSDT as an approximation of the mean elevation field $H(\mathbf{x})$ in Eq. (3). The climatological mean SSDT was calculated from climatological mean geopotential anomaly data (on 1°× 1°grid) at the sea surface relative to the 1000 dbar surface from all the hydrographic observation data compiled since 1907 by the Japan Oceanographic Data Center.

We prepared two different *in situ* observation data sets to evaluate the geoid improvement and the fluctuation SSDT. The first data set is location maps of the Kuroshio axis south of Japan inferred both from the geomagnetic electro-kinematograph (GEK) surface velocities and the horizontal temperature distribution in the upper layers. These maps are provided semimonthly in "Prompt Report on Oceanographic Conditions" issued by the Hydrographic Department of the Maritime Safety Agency, Japan. The second data set is the daily averaged sea levels recorded at tide gauge stations in the Japanese archipelago provided by the Japan Meteorological Agency and by the Hydrographic Department of the Maritime Safety Agency, Japan. First we determine the deviations from the temporal mean sea level over the first year of the Geosat ERM for each station, and then we average them over the same periods as the Geosat 17-day exact-repeat cycles to produce 17-day averaged fluctuation part of sea levels which is equivalent to the altimetric fluctuation SSDT ζ'_p.

5. Results

The temporal mean elevation field $H(\mathbf{x})$ relative to the improved geoid model (Imawaki *et al.*, 1991) in Eq. (4) is estimated by the optimal interpolation method described in Section 2 from the Geosat altimetry data southeast of Japan for the first year of ERM (Fig. 5). The figure shows that spatial variation of the mean sea levels is within the range of 1.8 m, which is much smaller than that referred to the geoid model before the improvement; the latter is more than 10 m (Imawaki *et al.*, 1991). Therefore, the errors $\varepsilon_N(\mathbf{r}) + \varepsilon_s(\mathbf{r})$ in the mean elevation field $H(\mathbf{x})$ is considered to be significantly reduced because of the geoid model improvement. In general, however, these errors still remain and are too large for the mean elevation field $H(\mathbf{x})$ to be used as the mean SSDT $\overline{\zeta}(\mathbf{x})$. Compared to the expected structure of the mean SSDT, the estimated elevation field $H(\mathbf{x})$ given in Fig. 5 shows too high values east of 145°E and too low values south of Japan (20°–30°N, 125°–140°E); both deviations from the expected structure are of the magnitude of several tens of centimeters. The mean elevation field $H(\mathbf{x})$, however, can be used as the mean SSDT $\overline{\zeta}(\mathbf{x})$ in the local area inside the thick dotted line in Fig. 5 where the geoid model was improved with contemporary hydrographic observations during the Seasat mission. Namely, the strong gradient of mean elevation field $H(\mathbf{x})$ south of Japan corresponds well to the expected structure of the mean SSDT $\overline{\zeta}(\mathbf{x})$ associated with the meandering Kuroshio, except for unrealistic longitudinal gradient at 28–30°N, 133–136°E, which is considered to be affected by the extreme low value centered just outside the boundary at 28°N, 133°E.

Fig. 5

Using the mean elevation field $H(\mathbf{x})$, the fluctuation SSDT relative to the one-year mean is estimated for 22 repeating 17-day cycles; as an example, the fluctuation SSDT ζ'_p for Cycle 2 is shown in Fig. 6. Since the mean elevation field $H(\mathbf{x})$ can be used as the mean SSDT $\overline{\zeta}(\mathbf{x})$ in the local area south of Japan, the absolute SSDT can be determined in the area by combining the mean elevation $H(\mathbf{x})$ and the fluctuation SSDT $\zeta'_p(\mathbf{x})$. Time series of the absolute SSDT from Cycles 1 to 6 are shown in Fig. 7

Fig. 6

Fig. 7

together with maps of estimated Kuroshio axis during corresponding periods determined by *in situ* observations. Both left and right panels, Fig. 7 (a)–(g) and (C1)–(C6), clearly describe the onset event of the large southward quasi-stationary meander of the Kuroshio. Namely, a small meander off Kii Peninsula centered at 33.5°N, 136–137°E in November, 1986 ((a)–(b) and (C1)–(C2)) rapidly grew in mid December to become a large narrow meander reaching its tip at 31°N, 140°E ((d) and (C3)). The meander gradually increased its width in January, 1987, which is remarked by the southward shift of the Kuroshio axis along 136°E ((f) and (C5)). The trail of the narrow meander can still be seen in Fig. 7 (C5) as a small southward distortion of the Kuroshio meander at the tip (31.5°, 139.5°E), but it was dismissed in the area in February, 1987 ((g) and (C6)). The small southward distortion of the meander in January, 1987 is not clear in the Kuroshio axis estimated from *in situ* observations (Fig. 7 (f)), but strong south-southeastward GEK velocity was recorded at 31°N, 139°E, which agrees well with the existence of the southward distortion of the axis. These good correspondences between the absolute SSDT and *in situ* observations reveal that both the mean SSDT $\overline{\zeta}(\mathbf{x})$ and the fluctuation SSDT $\zeta_p'(\mathbf{x})$ are accurately determined in this area, at least qualitatively. Quantitatively, geostrophic velocities determined from the absolute SSDT in the Kuroshio reach to the order of 1 m/s, the same order as the expected value. These velocities are in good agreement with surface velocities determined from trajectory data of a satellite-tracked drifting buoy; these comparisons will be described in a separated paper (Ichikawa *et al.*, 1995).

As described in the previous section, the tip of the large narrow meander seems to have been moved northeastward (Fig. 7 (C4)–(C5)) and dismissed in the area in February, 1987 (Fig. 7 (C6)). Time-longitude plot of the fluctuation SSDT at 31.5°N (Fig. 8) indicates that the tip was truncated from the meander and kept eastward movement with its magnitude being reduced; in the figure, it can be recognized as a somewhat fast (9 cm/s) eastward propagation of negative values (shown as a chain-line)

Fig. 8

appeared in Cycle 3 at 138.5°E, corresponding to the location of the tip of the narrow meander in Fig. 7 (d) and (C3). These eastward propagating negative values can be seen at 30°–33°N in the first half of the one-year period, and they seem to be merged in Cycles 12–13 with a westward propagating cyclonic ring detached from the Kuroshio Extension (Ichikawa and Imawaki, 1994). This eastward propagation is very unique since most of the fluctuation SSDT tends to show westward propagation (Tai and White, 1990; Aoki *et al.*, 1995), but its reason is not well understood.

In order to quantitatively evaluate the fluctuation SSDT, we compared it with daily mean sea-level tide gauge records. For eight tide gauge stations south of Japan (locations are shown in Fig. 9), the tide gauge fluctuation SSDT (hereinafter denoted by $\zeta'_p|_{tide}$) for each Geosat 17-day cycle is calculated as described in Section 4. On the other hand, values of the altimetric SSDT (ζ'_p) and its estimated error are extracted at the locations of the tidal stations by spatial bilinear interpolation of the closest four grid points. Figure 10 shows the comparisons of the fluctuation SSDT determined from the tide gauge records $\zeta'_p|_{tide}$ (dots) and that from the altimetry data ζ'_p (circles); basic statistics of those comparisons are summarized in Table 2. Here, the values of the altimetric fluctuation SSDT are not used when any one of the four closest grid points has an estimated error larger than 0.16 m; the values are also not displayed in Fig. 10 nor used for the calculations of the statistics. Uncertainty index (or an error bar in the figure) is chosen as the estimated error for the altimetric fluctuation SSDT ζ'_p, whereas the standard deviation of the 17-day average is used for the tide gauge fluctuation SSDT $\zeta'_p|_{tide}$.

Fig. 9

Fig. 10

Tab.2

In general, most of the pairs of altimetric and tide gauge fluctuation SSDT data are within the ranges of error bars of each other; the correlation coefficient of 0.49 for 140 comparisons is significant for t-test of 99.9% confidence level. This value is, however, smaller than those determined in similar comparisons in the tropical Pacific, 0.65–0.68 (Cheney *et al.*, 1989; Shibata and Kitamura, 1990). The reason for this lower correlation

is considered to be that the evaluation of the present analysis includes stations where the altimetric fluctuation SSDT cannot be obtained accurately. Some stations (Stations D–F) locate too close to large islands so that altimetry data near the stations cannot be sufficiently obtained comparing with stations in open ocean such as Stations A–C, G, and H or those in the tropical Pacific. At those tidal stations close to large islands, both the mean SSDT $\overline{\zeta}$ and the fluctuation SSDT ζ_p' determined from the altimetry data are less reliable; they can be marked by higher mean error values (12–13 cm) of the altimetric fluctuation SSDT ζ_p' (EA) in Table 2. The other reason for relatively poor comparisons is that time scale of dominant phenomena at some tidal stations may be too small to be resolved in the present altimetric fluctuation SSDT (ζ_p'). This is the case especially for Station G, which is marked with an distinctively high mean error value (12 cm) of the tide gauge fluctuation SSDT $\zeta_p'|_{tide}$ (ET) in Table 2, indicating rapid variations of sea levels within 17-days. The combined effect of rapid sea level variations together with insufficient altimetry data can be clearly shown in the panel of Station G in Fig. 10 during Cycles 18–20. During those periods, a strong cyclonic ring moving westward are known to have been coalesced to the Kuroshio at 33°N (Cycles 18–19) and advected to the east (Cycles 19–20) (Ichikawa and Imawaki, 1994). Namely, fast-moving small-scale structure was dominated in the variations of the fluctuation SSDT at Station G, which results in rapid decrease of the tide gauge fluctuation SSDT $\zeta_p'|_{tide}$ from Cycles 18 to 20 and increase from Cycles 20 to 22, with large error bars in Cycles 19–21. Meanwhile, most of the altimeter's descending along-track observations was missing during these periods so that the altimetric observations close to Station G were gathered only on the 14th day of the 17-day repeating cycle. As a result, the altimetric fluctuation SSDT ζ_p' was strongly weighted toward the latter half of the cycle; the altimetric fluctuation SSDT ζ_p' (circle) for each cycle during Cycles 18–20 in Fig. 10 is much closer to the tide gauge fluctuation SSDT $\zeta_p'|_{tide}$ (dot) of the next cycle rather than that of the same cycle. After Cycle 21 when a descending orbit on the 8th day of

the cycle was also available and when the cyclonic ring was completely away from the station, the error bar for the tide gauge fluctuation SSDT $\zeta'_p|_{tide}$is relatively small, and the agreement between circles and dots is better.

The other four stations (A–C and H), whose comparisons would be as reliable as those of the tidal stations in the tropical Pacific, show good agreements; correlation coefficient for these four stations is 0.60 (Table 2). However, the tilt (a) of the regression line ($\zeta'_p = a \times \zeta'_p|_{tide} + b$), 0.81, seems to be small even the effect of spatial smoothing on the altimetric fluctuation SSDT ζ'_p is taken into account, suggesting the existence of some systematic discrepancies still remained. Careful readers may have recognized the tendency that circles in Fig. 10 at any stations are generally higher than the corresponding dots in the first half of the entire period, whereas the situation is opposite in the second half. This tendency is more clearly shown in Fig. 11, a time series of the differences between a pair of the fluctuation SSDT's determined from the tide gauge records and from the altimetry data ($\zeta'_p|_{tide} - \zeta'_p$). The figure indicates that the differences are spatially systematic, and that they oscillate with a one-year period having a peak in late summer; the seasonal variation determined from all data plotted in Fig. 11 by the harmonic analysis is shown by a solid curve in the figure. This seasonal variation of the systematic differences is considered as the temporal variation of the areal average which is included in the tide gauge fluctuation SSDT $\zeta'_p|_{tide}$ but is lost in the altimetric fluctuation SSDT ζ'_p (see Section 3). Seasonal variation of the areal average over the present study field calculated from climatological monthly mean geopotential anomaly data (Teague *et al.*, 1990) is also plotted as dotted curve in Fig. 11, and its good agreement with the solid curve both in amplitude and phase confirms that losing the areal average in the altimetric fluctuation SSDT ζ'_p in each cycle is the cause of the seasonal variation of the systematic discrepancies. When the seasonal variation of the systematic differences (solid curve in Fig. 11) is added back to the altimetric fluctuation SSDT ζ'_p to compensate the loss of the areal averages, correlation coefficient (r) for those

Fig. 11

four stations increases up to 0.85, and the tilt (a) and bias (b) of the regression curve (Fig. 12) are improved to be 1.13 and -1.1 cm, respectively; the rms difference between the tide gauge and altimetric fluctuation SSDT's (VD) decreases to 6.0 cm. Fig. 12

6. Discussion

As described in Section 3, the random orbit error and the observation noise are expected to be removed from the input data by the optimal interpolation, retaining the oceanic signals except the spatial average height over the domain. In order to illustrate the results of these removals, we calculate a spatial covariance function over the domain ($C_{opt}(s)$) from the estimated fluctuation SSDT field, which includes contributions only from ζ'_p; here s denotes the distance lag. Then it is compared with another covariance function of the fluctuation SSDT processed through the conventional orbit reduction method; namely, the covariance function $\widehat{C}_{conv}(s)$ is calculated from the input altimetry data $R'(\mathbf{r}, t_p)$ in Eq. (5) after the conventional along-track tilt-and-bias orbit error removal procedure is applied (hereinafter, a symbol " $\widehat{\ }$ " indicates "with the tilt and bias removed"). Since the procedure also excludes tilt and bias heights of the oceanic signals, contributions included in $\widehat{C}_{conv}(s)$ are considered to be from oceanic signals of mid- and short-wavelength variations $\widehat{\zeta'_p}(\mathbf{r}) + \widehat{\zeta''_p}(\mathbf{r}, t_p)$ and from the random observation noise $\widehat{\varepsilon_m}(t_p)$ in Eq. 5 assuming that the orbit error was removed somewhat correctly by the conventional method. Both covariance functions are calculated for Cycle 2; for the calculation of $C_{opt}(s)$, values of the fluctuation SSDT field are extracted at the same data points as $\widehat{C}_{conv}(s)$ (Fig. 4). No data are used, however, along short (20 data points) subsatellite tracks; total number of data used to calculate the covariance is 777 points. Those covariance functions are plotted in Fig. 13 with normalization by the variance $C_{opt}(0)$ of $(0.12\ \mathrm{m})^2$. The variance $C_{opt}(0)$ is of reasonable value since that calculated from eight tide gauge records (total VT in Table 2) is $(0.11\ \mathrm{m})^2$. As seen in the figure, both covariance functions $C_{opt}(s)$ (solid line) and $\widehat{C}_{conv}(s)$ (dotted line) Fig. 13

behave in considerably different manner; for example, $\widehat{C}_{conv}(s)$, which is twice as large as $C_{opt}(0)$ at distance lag s of 0 km, suddenly decreases as lag s increases, while $C_{opt}(s)$ marks positive correlations for longer lag s so that the zero-crossing correlation length for $C_{opt}(s)$ of 800 km is four times larger than that of $\widehat{C}_{conv}(s)$ (200 km).

For the convenience of comparisons, we dare to exclude along-track tilt-and-bias oceanic signals from the fluctuation SSDT field ζ'_p and calculate another covariance function $\widehat{C}_{opt}(s)$ so that it includes contributions from $\widehat{\zeta'_p}$ rather than ζ'_p; the calculated covariance function is plotted by the broken line in Fig. 13. Comparing $\widehat{C}_{conv}(s)$ and $\widehat{C}_{opt}(s)$ which are expected to differ with contributions of $\widehat{\zeta''_p} + \widehat{\varepsilon_m}$, their discrepancy is found only at lag s of 0 km. The discrepancy is explained by the inclusion of contributions of $\widehat{\zeta''_p} + \widehat{\varepsilon_m}$ in the covariance function $\widehat{C}_{conv}(s)$; since these terms are expected to have random nature, their covariance function would behave like the Dirac-delta function at lag of 0 km for the present spatial resolution (67 km). Note that the variacne of these components of $(0.13\ \mathrm{m})^2$ estimated from $\widehat{C}_{conv}(0) - \widehat{C}_{opt}(0)$ is larger than that of ζ''_p of $(0.06\ \mathrm{m})^2$ calculated from the eight tide gauge records (total ET in Table 2), which suggests that the observation noise ε_m is of the magnitude of 0.12 m. On the other hand, the similarity of $\widehat{C}_{conv}(s)$ and $\widehat{C}_{opt}(s)$ for longer lag s confirms that the optimal interpolation does not alter the oceanic signal of mid-wavelength $\widehat{\zeta'_p}$ as expected from the test analysis in Section 3, and also that the discrepancy of $C_{opt}(s)$ and $\widehat{C}_{conv}(s)$ for $s \neq 0$ described above is caused by the removal of the tilt and bias of the oceanic signals. The latter indicates that statistics such as covariance functions would strongly depend on the accuracy of the orbit error reduction process.

The geoid improvement by combined use of Seasat altimetry data and hydrographic observations is excellent only in a local area south of Japan where *in situ* observations during three-month mission of Seasat exist. The reasons why the area outside still suffers relatively large errors are not explained clearly, but one of the candidates is an error introduced by substitution of the climatological mean SSDT for three-month

mean SSDT; many factors can be considered to cause discrepancies of these two means, including spatial changes of seasonal variations of sea levels, meso-scale phenomena such as Rossby waves, or changes of large-scale ocean circulation patterns. Use of longer-period mean elevation field $H(\mathbf{x})$ such as one determined in the present paper from one-year duration of Geosat altimetry data would relax the problem of substitution of the climatological mean. In addition, we may use enough contemporary hydrographic observations or results of reasonably reliable numerical models instead of substituting the climatological mean by limiting analysis to a small study area (Glenn *et al.*, 1991). One may also notice that unknown systematic orbit error $\varepsilon_s(\mathbf{x})$ could be another candidate of the error in the mean elevation field $H(\mathbf{x})$ since the orbit models used in Seasat and Geosat altimetry data are different so that the systematic orbit error $\varepsilon_s(\mathbf{x})$ would be different for each model. The effect of the systematic orbit error $\varepsilon_s(\mathbf{x})$ would be estimated by determining the mean elevation field $H(\mathbf{x})$ during the same period using another orbit height data set and comparing it with that determined in the present paper.

Comparisons with tide gauge records whose locations and time scale of sea-level variations are proper to evaluating the fluctuation SSDT ζ_p' show good agreement, indicating accurate determination of the fluctuation SSDT. Especially, when the areal average lost in the present optimal interpolation is added back, the comparison shows excellent agreement. One should note that temporal variation of the areal average for the first year of Geosat ERM (solid curve in Fig. 11) is almost the same as that determined from climatological mean seasonal variation (dotted curve in Fig. 11). This indicates that, if the study area is as wide as the present analysis case, we can use the areal average determined from the climatological mean seasonal variations without comparing tide gauge records as is performed in the present analysis. In addition, seasonal variations of the areal averages would be negligible for wider study area. Also note that the areal average of the SSDT field is not necessary to calculate geostrophic

velocities from it.

As exhibited in the comparisons of the tide gauge station G in Fig. 10, fast-moving small-scale features may cause spatio-temporal distortion of the estimated fluctuation SSDT field. It is impossible, however, to increase both temporal and spatial resolutions at the same time for any altimetry data set from a single satellite. Only the way to increase both resolutions is to analyze altimetry data sets from several satellites, such as combined use of ERS–1 and TOPEX/POSEIDON. Note that the optimal interpolation has no problem to consistently process these data sets of different accuracies and sampling patterns.

7. Summary

An optimal interpolation method is applied to Geosat altimetry data both to remove radial orbit error and to separate temporal mean sea surface dynamic topography (SSDT) from the fluctuations around the mean. The reliability of the method is first tested by artificial observation data, and it is found that the method can accurately reconstruct the SSDT field except for small scale structures and areal average component over the study area.

The temporally fluctuating part of SSDT (fluctuation SSDT) is quantitatively evaluated by eight tide gauge records on Japanese islands. The correlation coefficient between the tide gauge and altimetric fluctuation SSDT's is 0.49, which is significant for t-test of 99.9% confidence level. These comparisons includes, however, stations unfavorable for evaluation of the fluctuation SSDT, such as stations where altimetry data are sparse and stations where dominant sea-level variations are too rapid to be resolved by the present altimetry data set. Excluding such stations and recovering seasonal variations of the areal averages lost in the optimal interpolation, the correlation coefficient increases up to 0.85, and the tilt of the regression line becomes nearly the unity (1.13).

Also in the present paper, geoid model improvement by combined use of Seasat altimetry data and hydrographic observations (Imawaki *et al.*, 1991) is evaluated. In a local area where *in situ* observations contemporary to the Seasat altimetry mission exist, the improvement was excellent so that the absolute SSDT can be determined from altimetry data and the geoid model. Time series of the absolute SSDT describes the onset event of the quasi-stationary large meander of the Kuroshio south of Japan very well; namely, a small meander off Kii Peninsula rapidly grew to form a large narrow meander at the first stage, which gradually increased its width. The tip of the narrow meander moved eastward and seems to have been truncated from the large meander; analysis of time-longitude plot of the fluctuation SSDT at 31.5°N indicates that the truncated tip of the meander kept eastward movement at somewhat fast propagation speed of 9 cm/s.

Out of the local area south of Japan, however, the geoid model still includes unknown error of the order of several tens of centimeters. Substitution of climatological mean for the three-months mean during Seasat mission is considered to be one of the reason of this error.

Acknowledgments. We would like to thank Norihisa Imasato and colleagues of Department of Geophysics, Kyoto University for helpful overall discussions. Shigeru Aoki contributed to valuable discussions on interpretation of the results. Youichi Fukuda gave us valuable information and helpful suggestions about treatment of the geoid models. Most of the study was completed when K.I. was at Kyoto University and S.I. was at Kyoto University and Kagoshima University, Japan. The climatological mean geopotential anomalies for the western North Pacific were provided by the Japan Oceanographic Data Center; Tomotaka Ito made the calculations. Data were processed on a FACOM computer at the Data Processing Center of Kyoto University. The figures were produced by GFD–DENNOU Library. This research was supported in part by a Grant-in-Aid for Scientific Research from the Ministry of Education, Science and Culture, Japan.

References

Aoki, S., S. Imawaki and K. Ichikawa (1995): Baroclinic disturbances propagating westward in the Kuroshio Extension region as seen by a satellite altimeter and radiometers. *J. Geophys. Res.*, **100**(C1), in press.

Bretherton, F.P., R.E. Davis and C.B. Fandry (1976): A technique for objective analysis and design of oceanographic experiments applied to MODE-73. *Deep Sea Res.*, **23**, 559-582.

Cheney, R.E., J.G. Marsh, and B.D. Beckley (1983): Global mesoscale variability from collinear tracks of Seasat altimeter data. *J. Geophys. Res.*, **88**(C7), 4343–4354.

Cheney, R.E., B.C. Douglas, R.W. Agreen, L. Miller, D.L. Porter, and N.S. Doyle (1987): *Geosat altimeter geophysical data record user handbook.* NOAA Tech. Memo. NOS NGS-46, U.S. Govt. Print. Office, Washington, D.C., 29 pp.

Cheney, R.E., B.C. Douglas and L. Miller (1989): Evaluation of Geosat altimeter data with application to tropical Pacific sea level variability. *J. Geophys. Res.*, **94**(C4), 4737–4747.

Ganeko, Y. (1983): A 10' × 10' detailed gravimetric geoid around Japan. *Marine Geodesy*, **7**, 291–314.

Glenn, S.M., D.L. Porter, and A.R. Robinson (1991): A synthetic geoid validation of Geosat mesoscale dynamic topography in the Gulf Stream region. *J. Geophys. Res.*, **96**(C4), 7145–7166.

Haines, B.J., G.H. Born, G.W. Rosborough, J.G. Marsh, R.G. Williamson (1990): Precise orbit computation for the Geosat Exact Repeat Mission. *J. Geophys. Res.*, **95**(C3), 2871–2885.

Ichikawa, K. and S. Imawaki (1992): Fluctuation of sea surface dynamic topography southeast of Japan estimated from Seasat altimetry data. *J. Oceanogr.*, **48**, 155–177.

Ichikawa, K. and S. Imawaki (1994): Life history of a cyclonic ring detached from the Kuroshio Extension as seen by the Geosat altimeter. *J. Geophys. Res.*, **99**(C8), 15,953–15,966.

Ichikawa, K., S. Imawaki and H. Ishii (1995): Comparisons of altimetry-derived geostrophic velocities and surface velocities determined from drifting buoy trajectory south of

Japan. in preparation.

Imawaki, S., K. Ichikawa and H. Nishigaki (1991): Mapping the mean sea surface elevation field from satellite altimetry data using optimal interpolation. *Marine Geodesy*, **15**, 31–46.

Koblinsky, C.J., Gaspar, P. and G. Lagerloef (1992), editors: *The future of spaceborne altimetry: Oceans and climate change.* Joint Oceanographic Institutions Incorporated, Washington, D.C., 75pp.

Lerch, F.J., J.G. Marsh, S.M. Klosko and R.G. Williamson (1982): Gravity model improvement for SEASAT. *J. Geophys. Res.*, **87**(C5), 3281-3296.

Mazzega, P. and S. Houry (1989): An experiment to invert Seasat altimetry for the Mediterranean and Black Sea mean surfaces. *Geophys. J.*, **96**, 259-272.

Nerem, R.S., B.D. Tapley, and C.K. Shum (1990): Determination of the ocean circulation using Geosat altimetry. *J. Geophys. Res.*, **95**(C3), 3163–3179.

Rapp, R.H., and Y.M. Wang (1994): Dynamic topography estimates using Geosat data and a gravimetric geoid in the Gulf Stream region. *Geophys. J. Int.*, **117**, 511–528.

Shibata A. and Y. Kitamura (1990): Geosat sea level variability in the tropical Pacific in the period from November 1986 to February 1989, obtained by collinear method. *Oceanogr. Mag.*, **40**, 1–26.

Tai, C.-K., and W.B. White (1990): Eddy variability in the Kuroshio Extension as revealed by Geosat altimetry: Energy propagation away from the jet, Reynolds stress, and seasonal cycle. *J. Phys. Oceanogr., 20*, 1761–1777.

Tapley, B.D., G.H. Born and M.E. Parke (1982): The SEASAT altimeter data and its accuracy assessment. *J. Geophys. Res.*, **87**(C5), 3179-3188.

Teague, W.J., M.J. Carron, P.J. Hogan (1990): A comparison between the generalized digital environmental model and Levitus climatologies. *J. Geophys. Res.*, **95**(C5), 7167–7183.

Thiébaux, H.J. and M.A. Pedder (1987): *Spatial Objective Analysis: With Applications in Atmospheric Science.* Academic Press, London, 299 pp.

Wagner, C.A. and C.K. Tai (1994): Degradation of ocean signals in satellite altimetry due to orbit error removal processes. *J. Geophys. Res.*, **99**(C8), 16255–16267.

Wunsch, C. (1986): Calibrating an altimeter: How many tide gauges is enough? *J. Atmos. and Oceanic Tech.*, **3**, 746-754.

Wunsch, C. and V. Zlotnicki (1984): The accuracy of altimetric surfaces. *Geophys. J. Roy. Astron. Soc.*, **78**, 795-808.

This manuscript was prepared with the AGU LaTeX macros v3.1.

Geosat 高度計データから求めた日本近海での海面力学高度の時間変動

市川 香*, 今脇資郎†

要旨

最適内挿法を使用して、Geosat 高度計のデータから海面力学高度の時間変動成分を精度よく求めた。得られた時間変動成分を、日本周辺の八つの検潮所における日平均水位データと比較すると、両者の相関係数は 0.49 であった。このうち、高度計の時間変動成分の推定精度の悪い検潮所を除き、さらに最適内挿法によって失われる海域全体にわたる季節変動成分を補うと、相関係数は 0.85 まで向上した。また、Seasat 高度計データを使って改良されたジオイド・モデルの評価を行った。Seasat の海面高度観測と同時期に海洋観測が行われていた海域では、モデルは十分な精度で改良されており、高度計データから直接求めた絶対海面力学高度場によって、黒潮が非蛇行流路から定常蛇行流路へと遷移していく様子を克明に記述することができた。しかし、それ以外の領域では、モデルの改良は不十分であることが分かった。

*愛媛大学工学部土木海洋工学科 〒790–77 愛媛県松山市文京町 3

†九州大学応用力学研究所 〒816 福岡県春日市春日公園 6–1

Fig. 1. An example of the optimal interpolation performance tests. The true field superimposed on the data points (after 10-points averaging) (a) and the reconstructed field (b) are shown. Note that the structure in panel (a) is almost correctly reconstructed in panel (b) but with slight distortion. Parameters in formula (9) for panel (a) are $N = 1$, $\alpha = 0.4$ m (rms height of the signal is 0.2 m), $L_x = 490$ km, $L_y = 600$ km and $\beta = 0.02$ m (rms height of the noise is 0.02 m). Parameters for the optimal interpolation for panel (b) are $w_0 = 0.2$ m, $L = 150$ km and $\sigma_0 = 0.02$ m. Contour and shading intervals are 0.1 m and lower values are shaded more heavily; zero level is indicated by thick contour lines and negative values are shown with dotted contour lines. Resolution of both panels is $0.25° \times 0.25°$. In panel (b), contours and shading are omitted at points where the estimated error exceeds 0.05 m in order to exclude unreliable estimates.

Fig. 2. The rms difference (solid line) between the true field and the reconstructed field plotted against various L_y (in km) keeping the ratio $L_x/L_y = 0.82$; other parameters used are the same as Fig. 1. Rms differences for cases of L_y smaller than 300 km are not plotted since their reconstructed fields are dominated by structures whose wavelengths are different from those of the true field. Also in the figure, rms height of the reconstructed field are plotted (crosses). In the calculations of both rms height and rms difference, unreliable estimates indicated by higher estimated errors are not used.

Fig. 3. The rms difference between the true field and the reconstructed field plotted against the ratio w_0/σ_0. Solid line is for artificial input observation data with $\alpha = 0.2$ m and $\beta = 0.02$ m, whereas dotted line is for data with $\alpha = 0.2$ m and $\beta = 0.2$ m. Other parameters used are the same as Fig. 1. Signal to noise ratios of the input data (after 10 point averaging) are indicated on the abscissa by open (for solid line) and closed (for dotted line) triangles. In the calculations of rms difference, unreliable estimates indicated by higher estimated errors are not used.

Fig. 4. Data points distribution for Geosat ERM Cycle 2. Dotted line indicates the boundary of the study area.

Fig. 5. Temporal mean elevation field $H(\mathbf{x})$ relative to the improved geoid model (Imawaki *et al.*, 1991) estimated on a 0.5°× 0.5°grid. Contour and shading intervals are both 0.2 m, but they are gapped by 0.1 m; area of lower values is shaded more heavily. Inside the thick broken line, contemporary hydrographic observation data were used in the geoid model improvement. Contours and shading are omitted at points where the estimated error exceeds 0.3 m.

Fig. 6. An example (Cycle 2) of the fluctuation SSDT estimated on a 0.5°× 0.5°grid. Contour and shading intervals are 0.1 m and lower values are shaded more heavily; zero level is indicated by thick contour lines and negative values are shown with dotted contour lines.

Fig. 7. Maps of the Kuroshio axis determined from *in situ* oceanographic observations for early November 1986 (a) to early February, 1987 (g) (partial copies of "Prompt Report on Oceanographic Conditions" issued semimonthly by the Hydrographic Department of the Martime Safety Agency, Japan); small arrows indicate GEK surface velocities. Maps of the absolute SSDT (the mean elevation $H(\mathbf{x})$ plus the fluctuation SSDT $\zeta'_p(\mathbf{x})$) from Cycle 1 (C1) to Cycle 6 (C6) are shown to the right of the center line; contour and shading intervals are 0.2 m with 0.1 m gap for each other, and lower values are shaded more heavily. Positions of all panels are shifted from top to bottom according to the central date of the observation periods.

Fig. 8. Time-longitude plot of the fluctuation SSDT at latitude 31.5°N. In the figure, seasonal variations at each longitude are removed in order to highlight meso-scale variations. Contour and shading intervals are 0.1 m and lower values are shaded more heavily; zero level is indicated by thick contour lines and negative values are shown with dotted contour lines. Contours and shading are omitted at points where the estimated error of the fluctuation SSDT exceeds 0.16 m. Left scale indicates the observation dates and right scale indicates cycle numbers. Chain-line is plotted for convenience of discussions.

Fig. 9. Locations of tide gauge stations used in the comparisons of the altimetric and tide gauge fluctuation SSDT's in Fig. 10. They are Ishigaki (A), Naha (B), Naze (C), Nishino-omote (D), Kushimoto (E), Minami-izu (F), Hachijo-jima (G) and Chichi-jima (H).

Fig. 10. Comparisons of fluctuation SSDT's estimated from the tide gauge records $\zeta'_p|_{tide}$ (dots) and from the Geosat altimetry data ζ'_p (circles). Vertical lines are error bars. Estimates of ζ'_p are not shown when any of the estimated errors at the closest four grid points exceeds 0.16 m, and estimates of $\zeta'_p|_{tide}$ are not shown when the cycle mean is estimated from less than 8-day records. Numerals in the abscissa are cycle numbers, and those in the ordinate are height in cm.

Fig. 11. Differences (in cm) between the tide gauge and altimetric fluctuation SSDT's $(\zeta'_p|_{tide} - \zeta'_p)$ for Stations A (circles), B (squares), C (triangles) and H (crosses) plotted against cycles (upper scale) or the time of observations (lower scale). Solid curve indicates a least-squared-fitted sinusoidal curve of one-year period. Dotted curve indicates a climatological mean seasonal variation of the areal averaged sea surface dynamic height.

Fig. 12. Scatter plots of the tide gauge and altimetric fluctuation SSDT's for Stations A (circles), B (squares), C (triangles) and H (crosses) before (a) and after (b) the compensation of the seasonal variation of the areal averages. The regression lines are also drawn in the figures.

Fig. 13. Comparison of spatial covariance functions over the domain; they are the covariance function $C_{opt}(s)$ (solid line) determined from the fluctuation SSDT field ζ'_p, $\widehat{C}_{conv}(s)$ (dotted line) determined from the altimetry data $\widehat{\zeta'_p} + \widehat{\zeta''_p} + \widehat{\varepsilon_m}$ processed with along-track bias-and-tilt orbit removal, and $\widehat{C}_{opt}(s)$ (broken line) determined from the fluctuation SSDT field with along-track bias-and-tilt oceanic signals excluded, $\widehat{\zeta'_p}$. All functions are normalized by $C_{opt}(0)$, $(0.12\ \mathrm{m})^2$; spatial resolution of those functions is 67 km.

Table 1. Number of data points (after 10-point averaging), and start and end dates of each cycle.

Cycle Number	Start and End Dates	Number of Data
1	Nov. 8 – 24, 1986	727
2	Nov. 25 – Dec. 11, 1986	1015
3	Dec. 12 – 28, 1986	974
4	Dec. 29, 1986 – Jan. 14, 1987	935
5	Jan. 15 – 31, 1987	921
6	Feb. 1 – 17, 1987	715
7	Feb. 18 – Mar. 6, 1987	701
8	Mar. 7 – 23, 1987	790
9	Mar. 24 – Apr. 9, 1987	827
10	Apr. 10 – 27, 1987	865
11	Apr. 28 – May 14, 1987	959
12	May 15 – 31, 1987	900
13	Jun. 1 – 17, 1987	753
14	Jun. 18 – Jul. 4, 1987	734
15	Jul. 5 – 21, 1987	454
16	Jul. 22 – Aug. 7, 1987	607
17	Aug. 8 – 24, 1987	636
18	Aug. 25 – Sep. 10, 1987	489
19	Sep. 11 – 27, 1987	601
20	Sep. 28 – Oct. 14, 1987	664
21	Oct. 15 – 31, 1987	909
22	Nov. 1 – 17, 1987	858

Table 2. Statistics of the fluctuation SSDT determined from the tide gauge records ($\zeta'_p|_{tide}$) and from the Geosat altimetry data (ζ'_p) (Fig. 10) at each tide gauge station (Fig. 9). They include number of data (n) used in this comparison, rms of $\zeta'_p|_{tide}$ (VT), that of ζ'_p (VA), rms of their differences (VD), mean errors (error bars in Fig. 10) of $\zeta'_p|_{tide}$ (ET), those of ζ'_p (EA), correlation coefficient (r) between $\zeta'_p|_{tide}$ and ζ'_p, tilt (a) and bias (b) of regression lines; $\zeta'_p = a \times \zeta'_p|_{tide} + b$. All values are in centimeter except for nondimensional values of n, r and a.

Station	n	VT	VA	VD	ET	EA	r	a	b
A	19	11.2	11.6	10.3	4.4	10.9	0.60	1.06	1.5
B	20	10.4	6.8	6.7	3.7	11.4	0.78	0.58	-1.5
C	18	10.1	9.3	8.7	4.2	10.6	0.60	0.87	-3.1
D	14	10.4	11.1	10.3	5.6	12.7	0.54	1.11	-3.1
E	19	7.0	12.1	12.7	6.3	12.2	0.20	5.94	3.8
F	6	3.3	8.7	7.4	6.4	12.9	0.55	4.31	3.8
G	22	16.2	13.9	16.2	12.0	11.2	0.43	0.70	-1.6
H	22	9.1	7.8	8.5	4.4	10.7	0.50	0.74	-0.0
Total	140	10.8	10.5	10.9	5.9	11.4	0.49	0.94	-1.6
Subtotal for A–C and H	79	10.2	9.0	8.6	4.2	10.9	0.60	0.81	-0.9

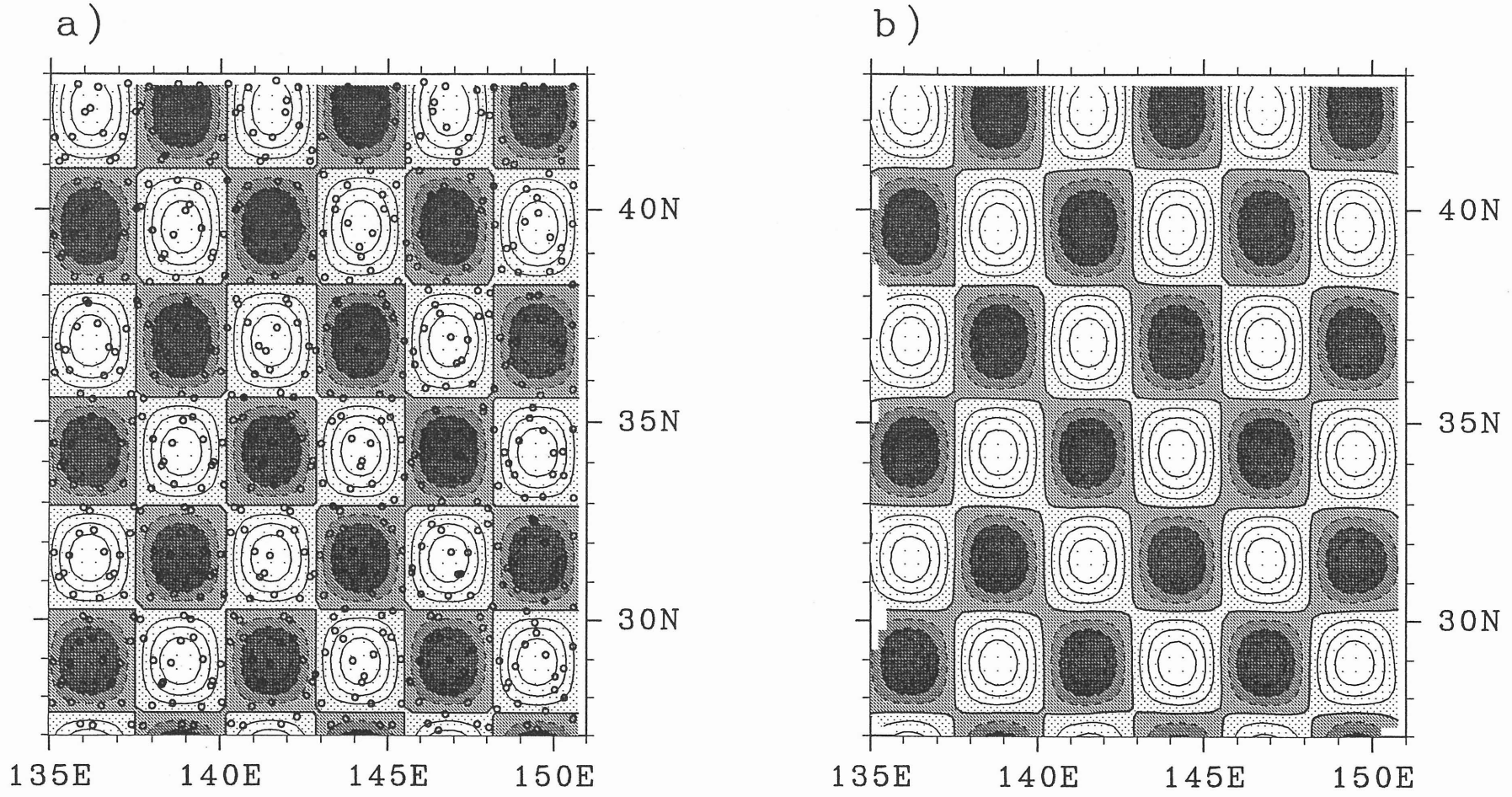

Fig 1 Ichikawa and Imawaki

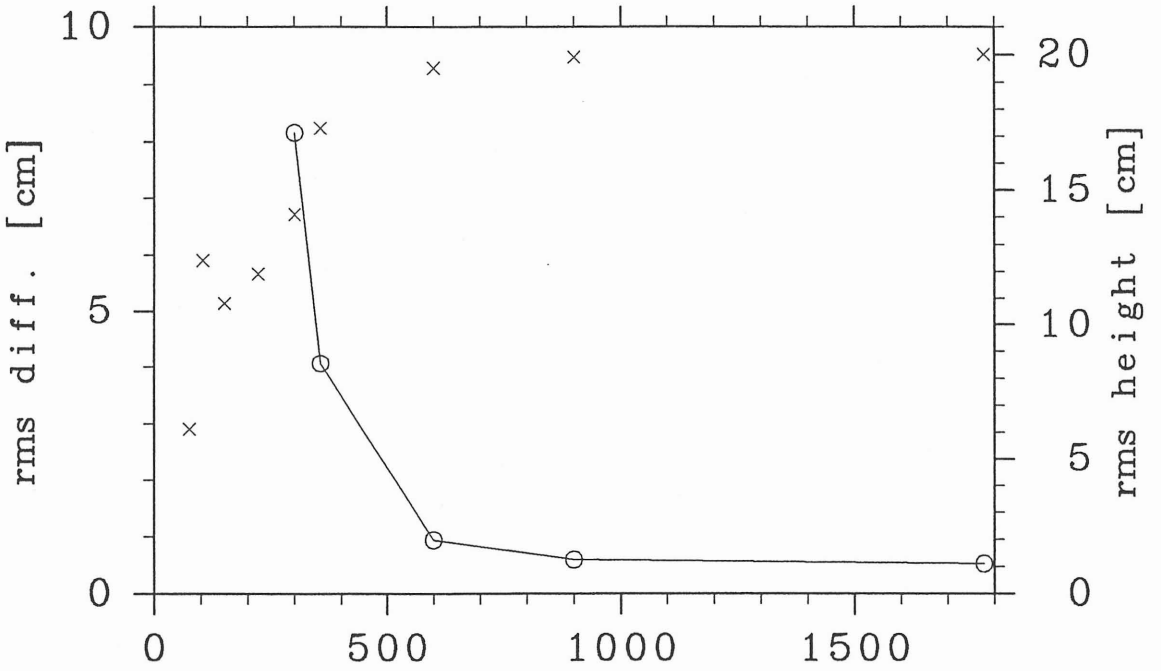

Fig 2 Ichikawa and Imawaki

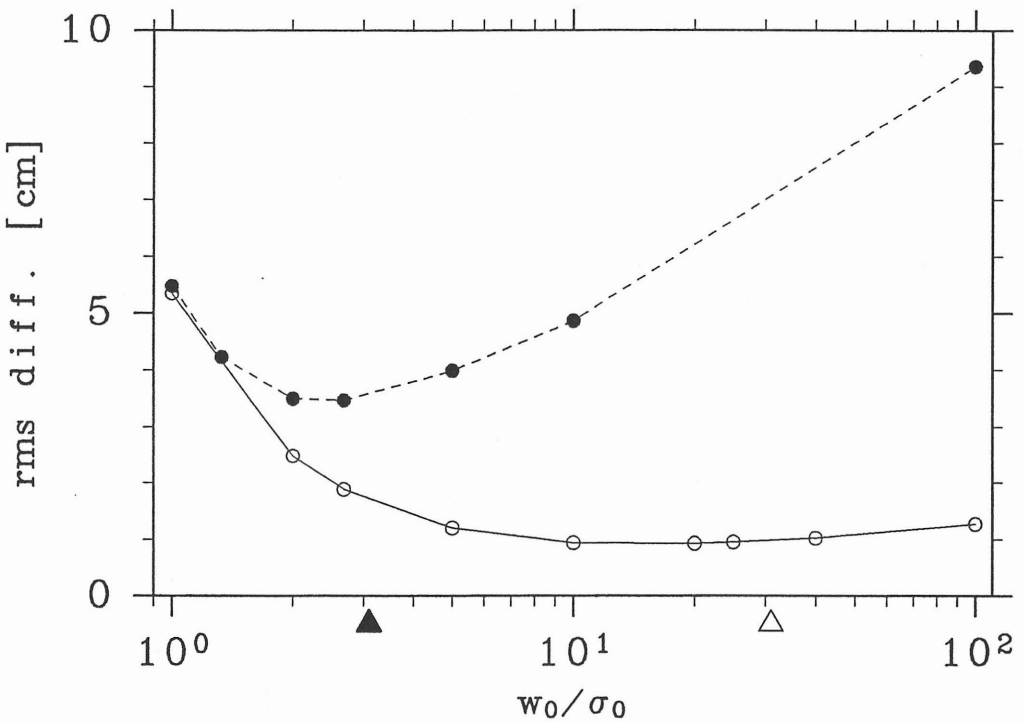

Fig 3 Ichikawa and Imawaki

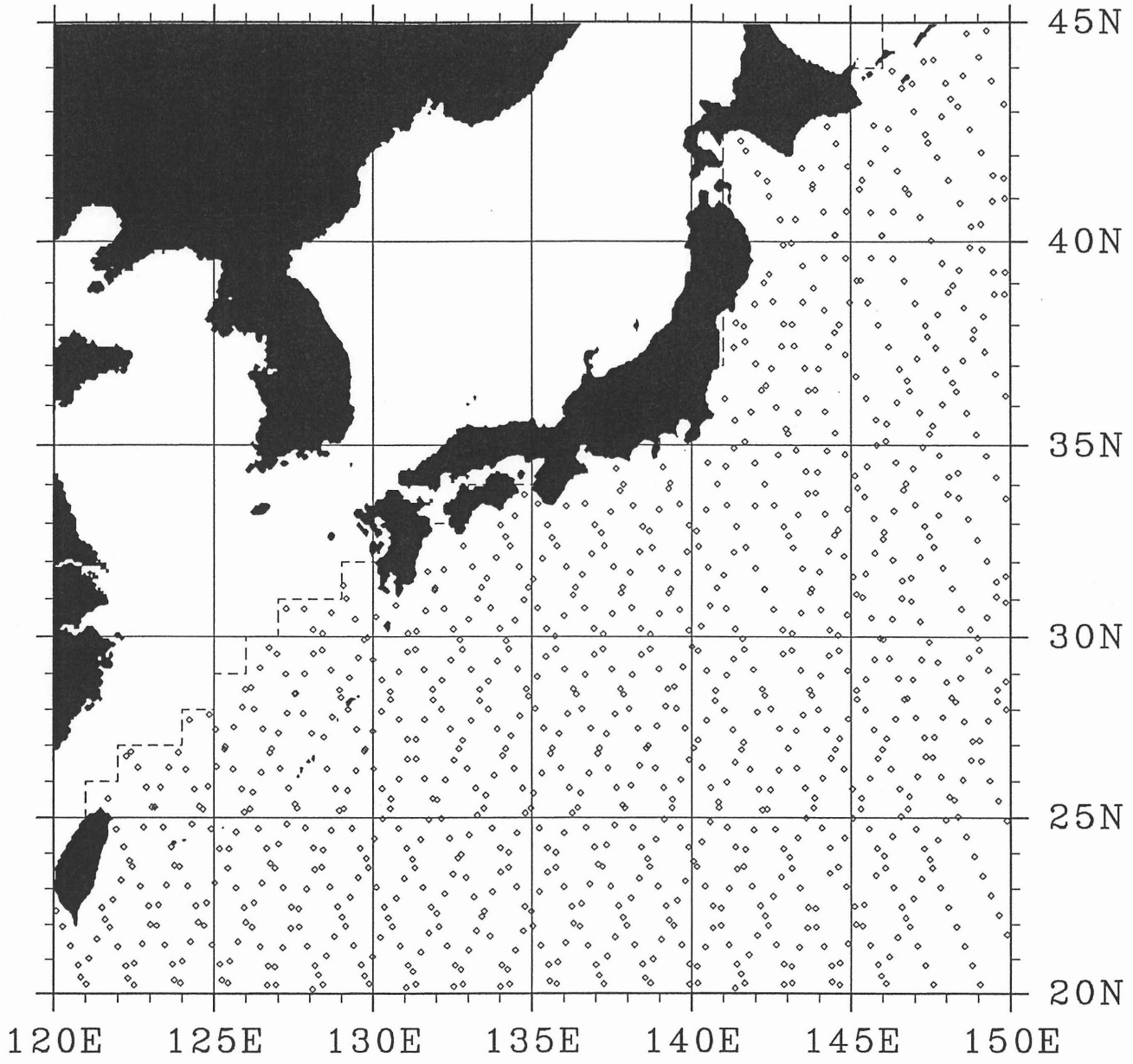

Fig 4

Ichikawa and Imawaki

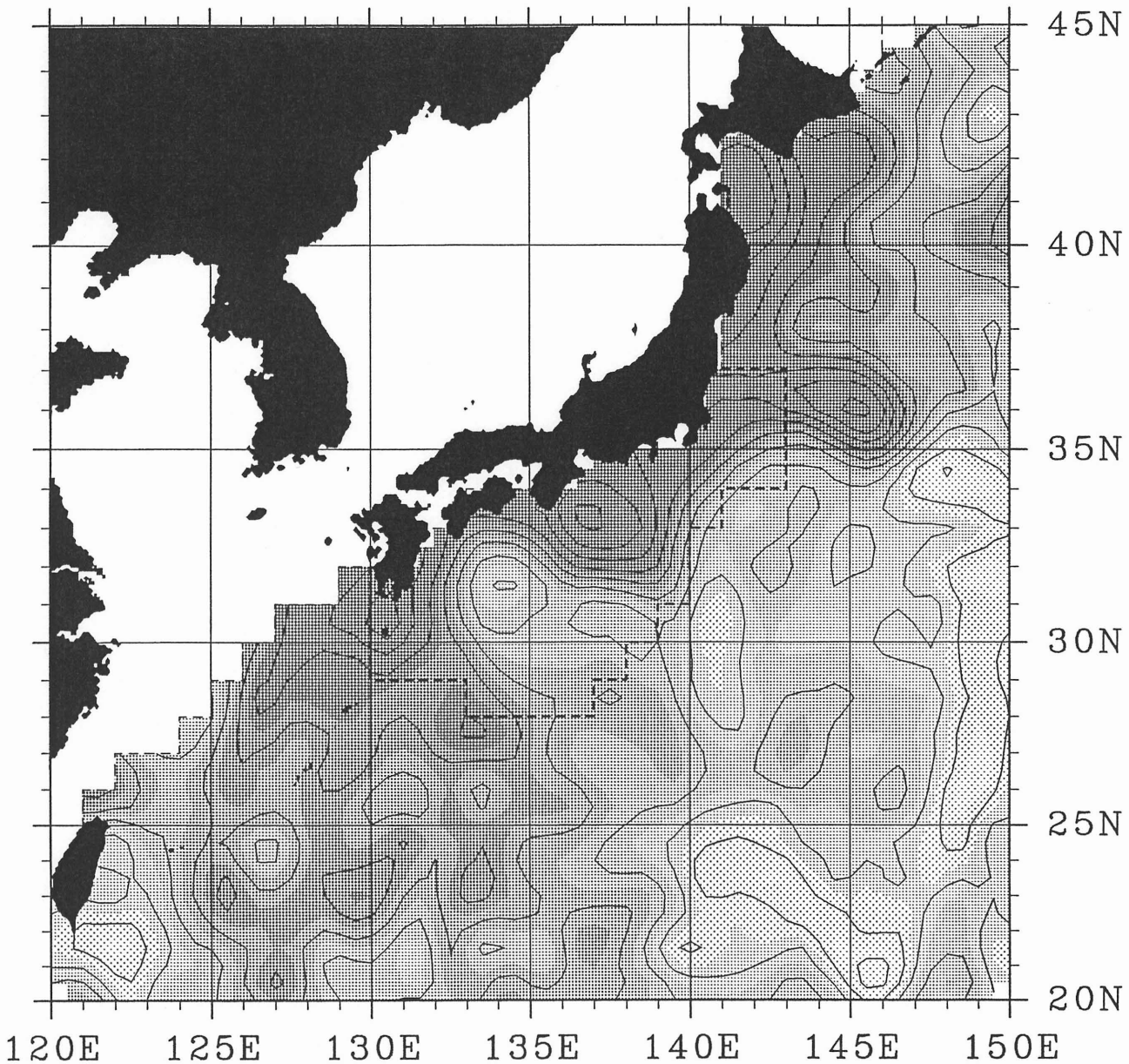

Fig 5 Ichikawa and Iwawaki

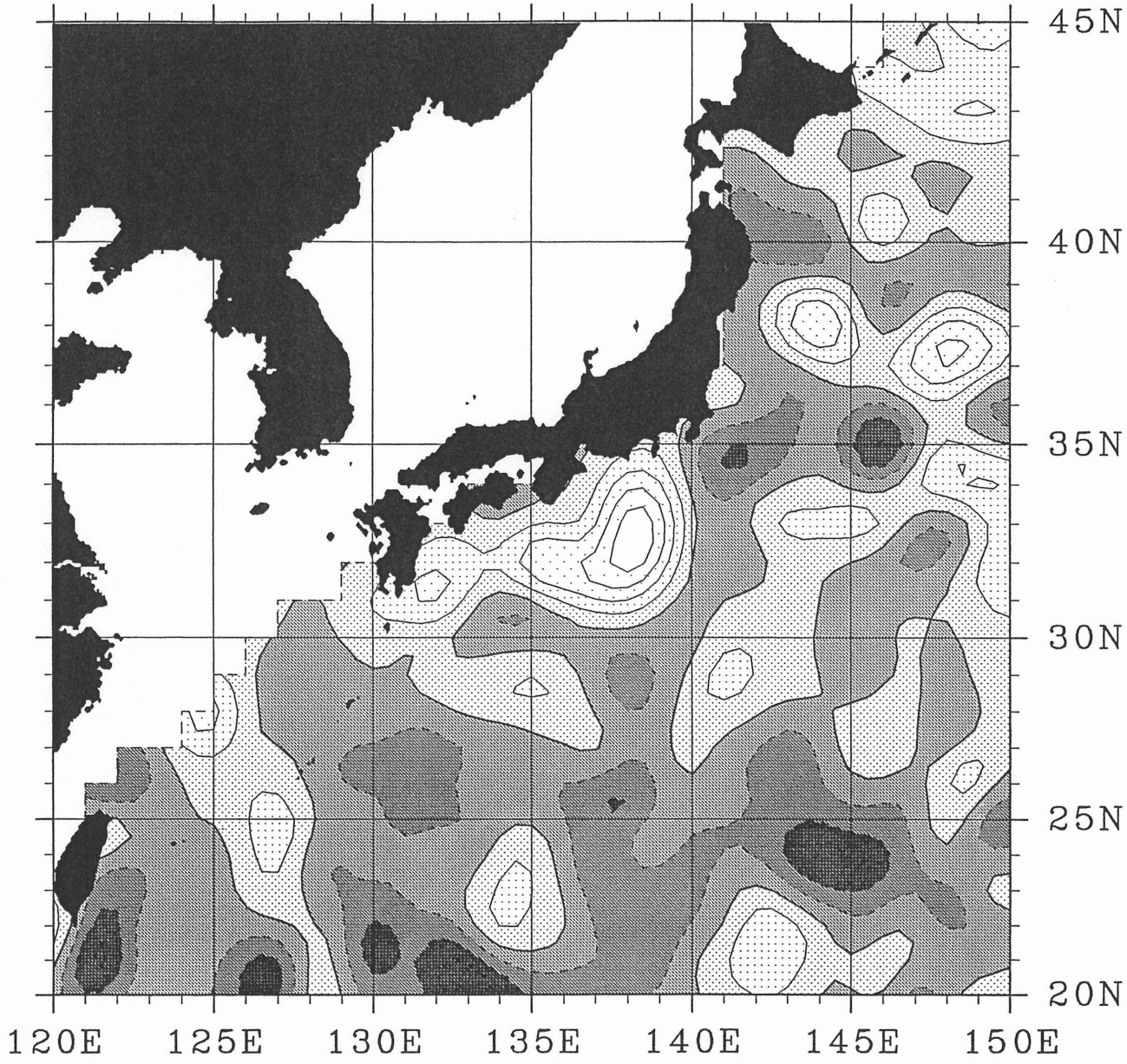

Fig 6

Ichikawa and Imawaki

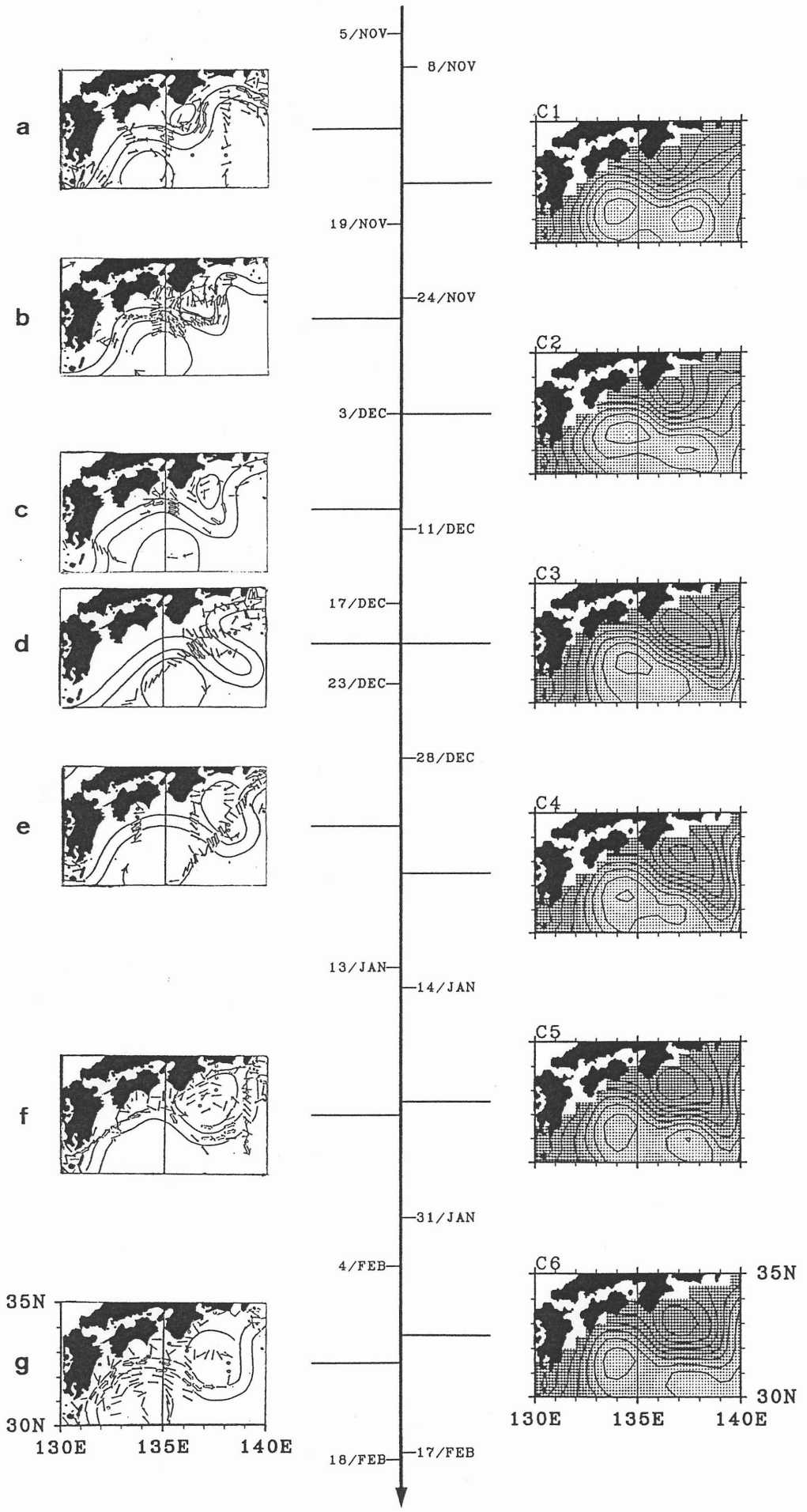

Ichikawa and Imawaki

Fig 7

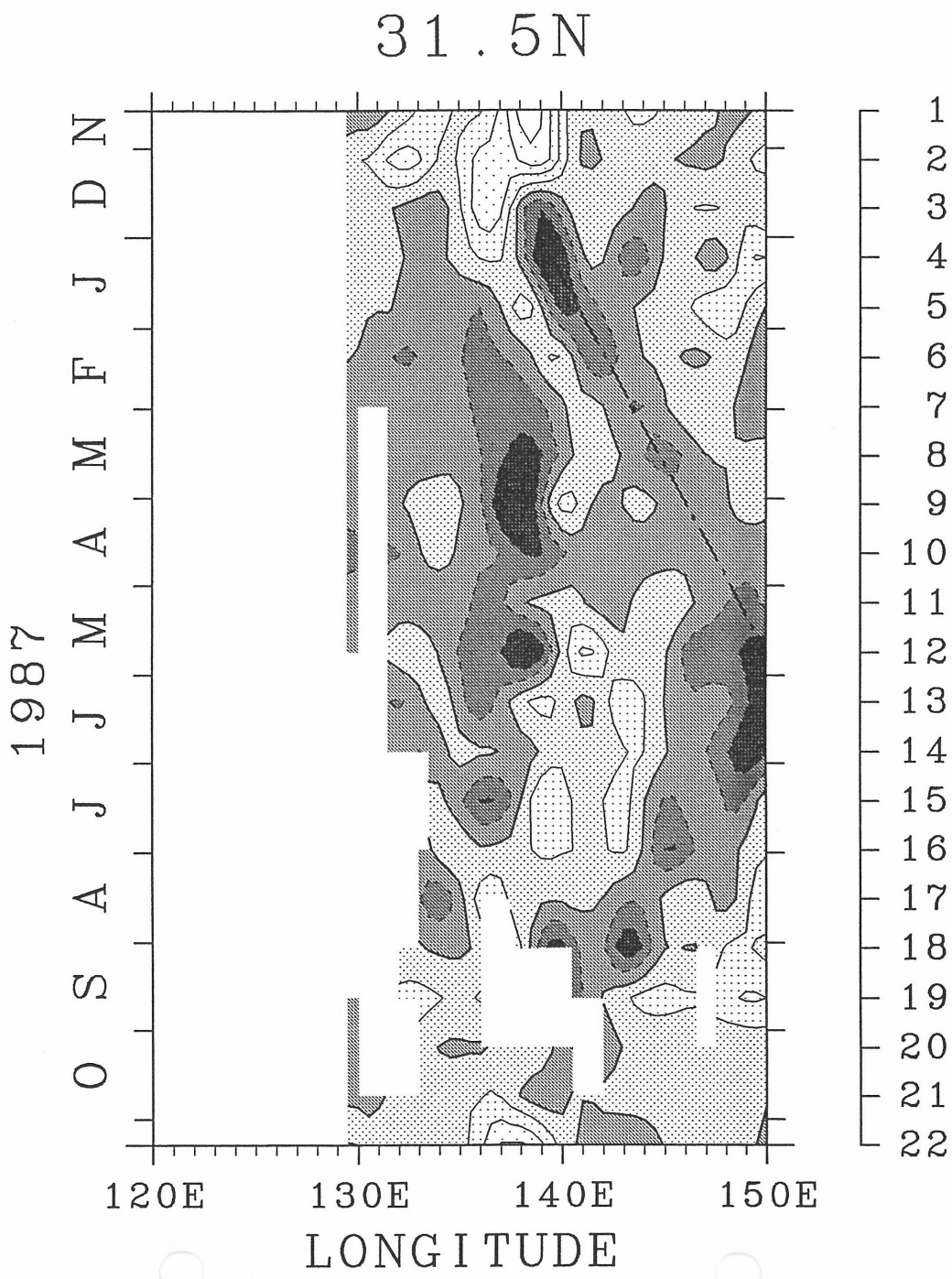

Ichikawa and Imawaki

Fig 8

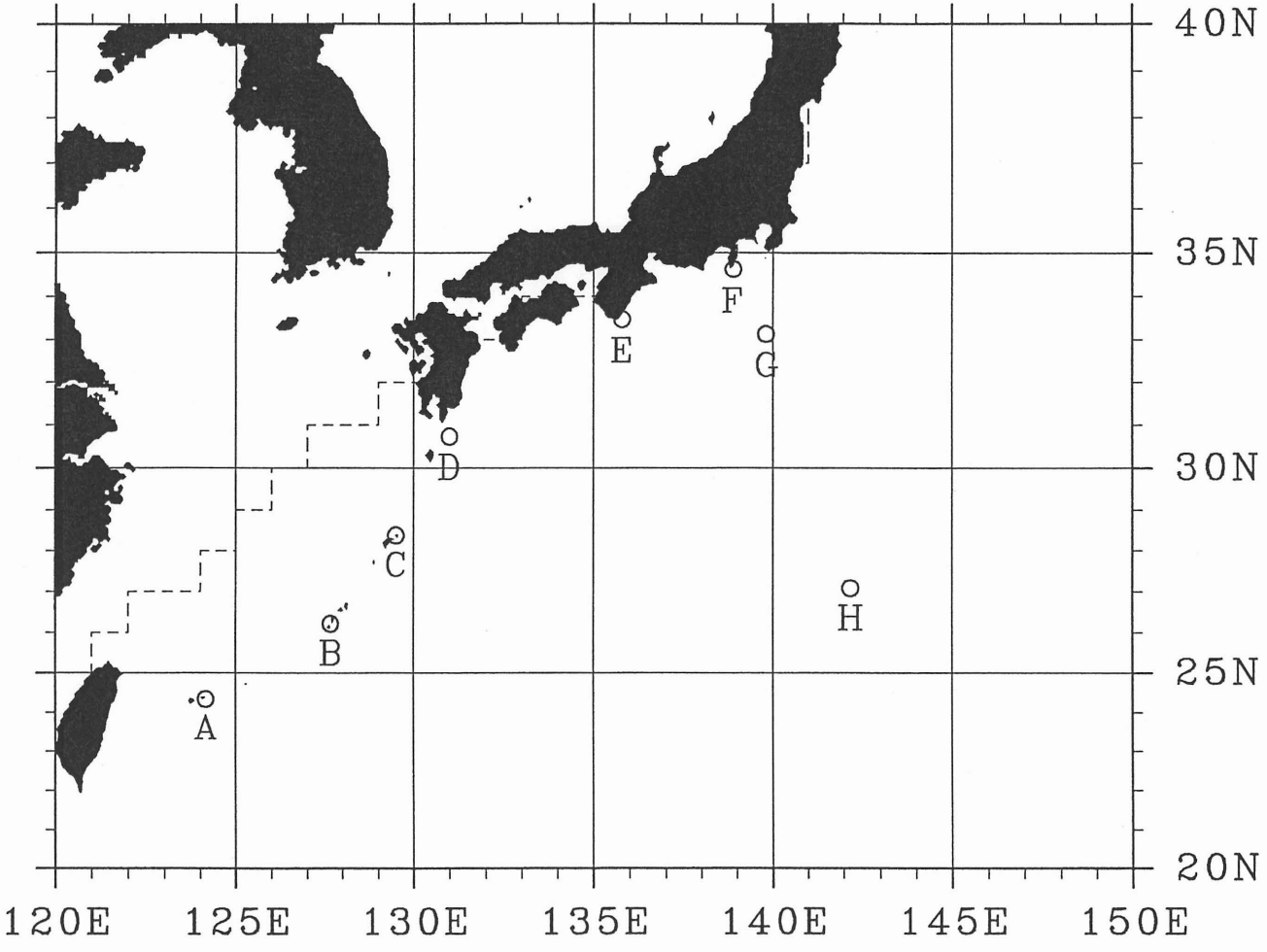

Ichikawa and Imawaki

Fig 9

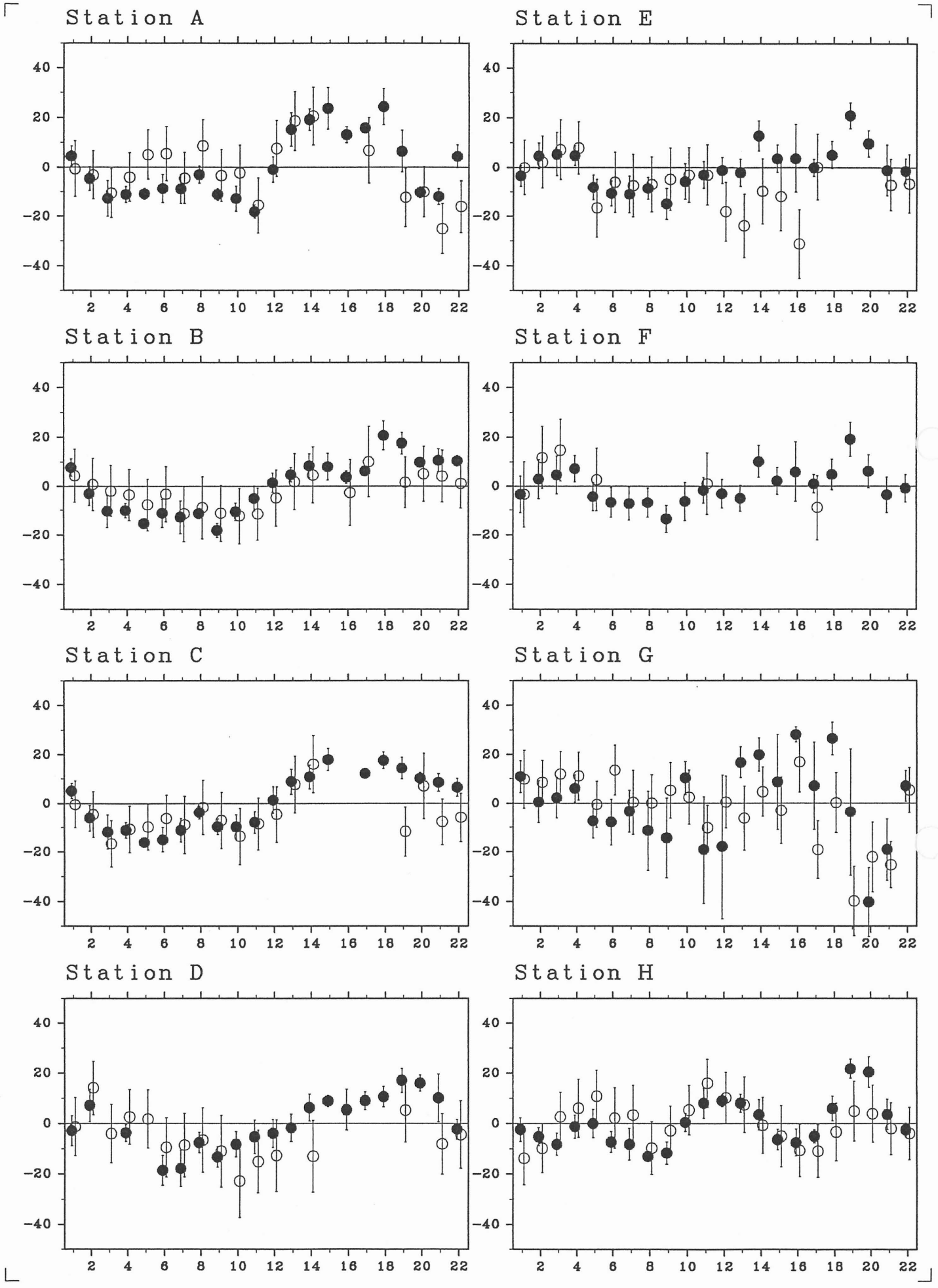

Fig 10 Ichikawa and

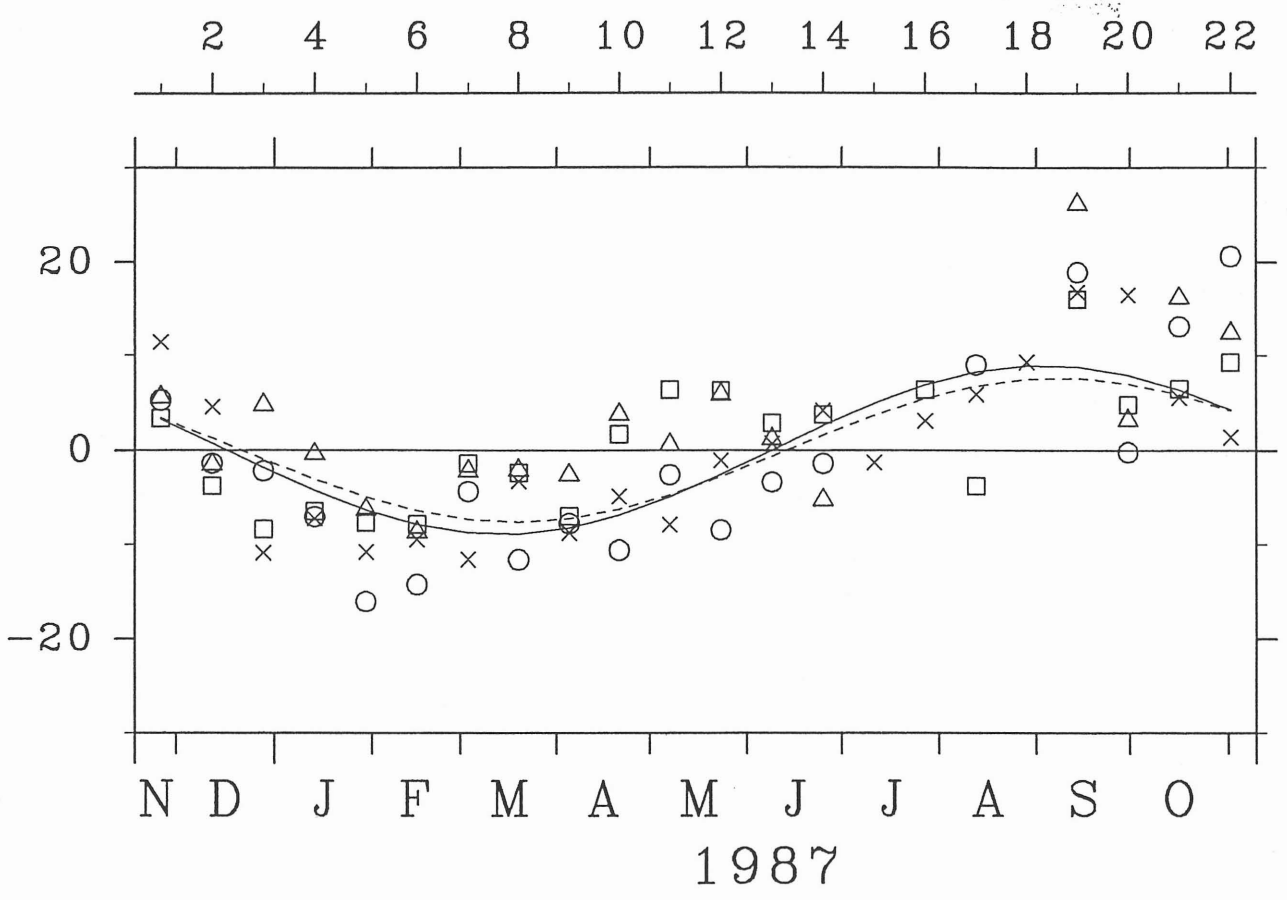

Fig 11

Ichikawa and Imawaki

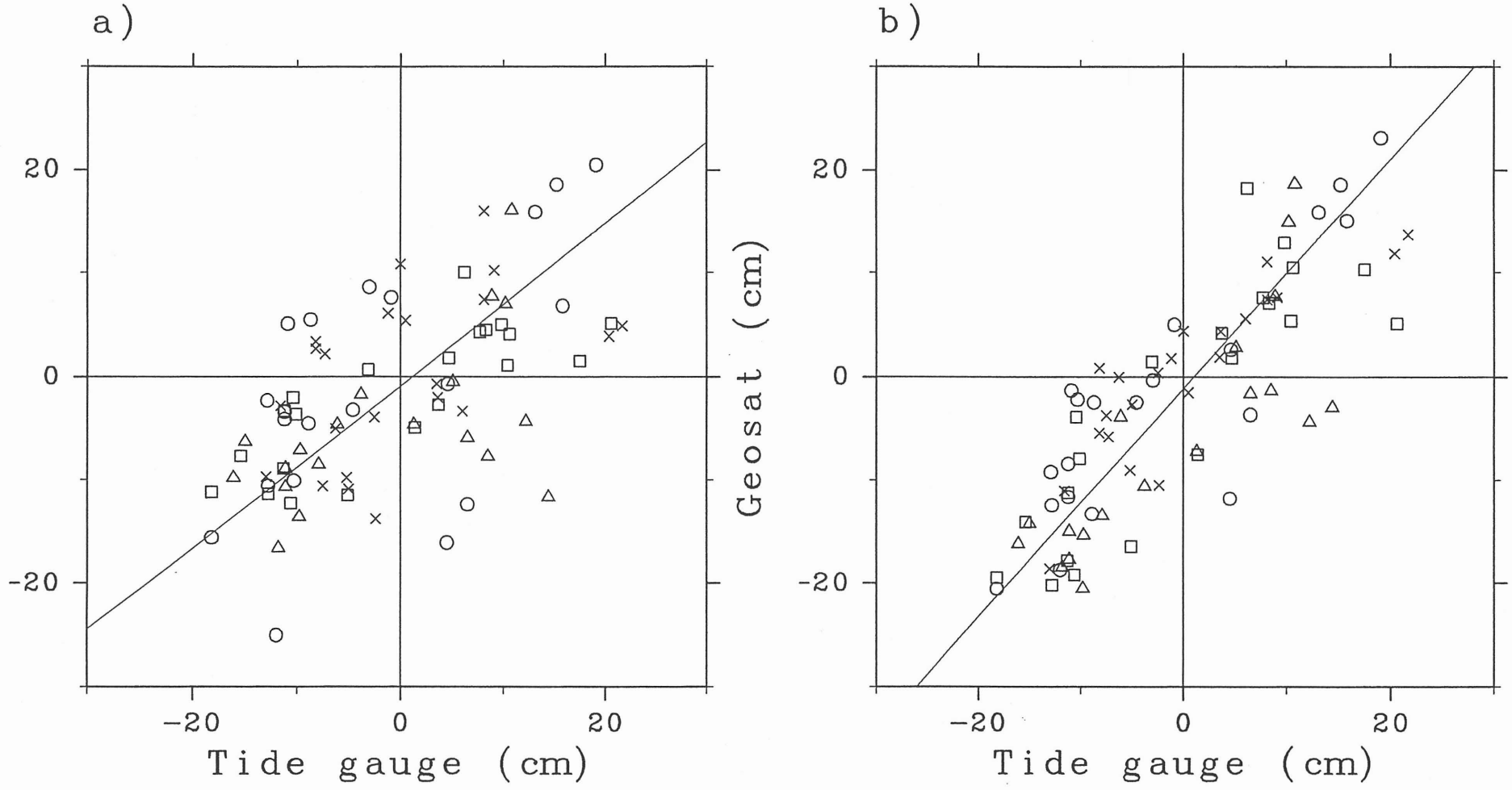

Fig 12 Ichikawa and Imawaki

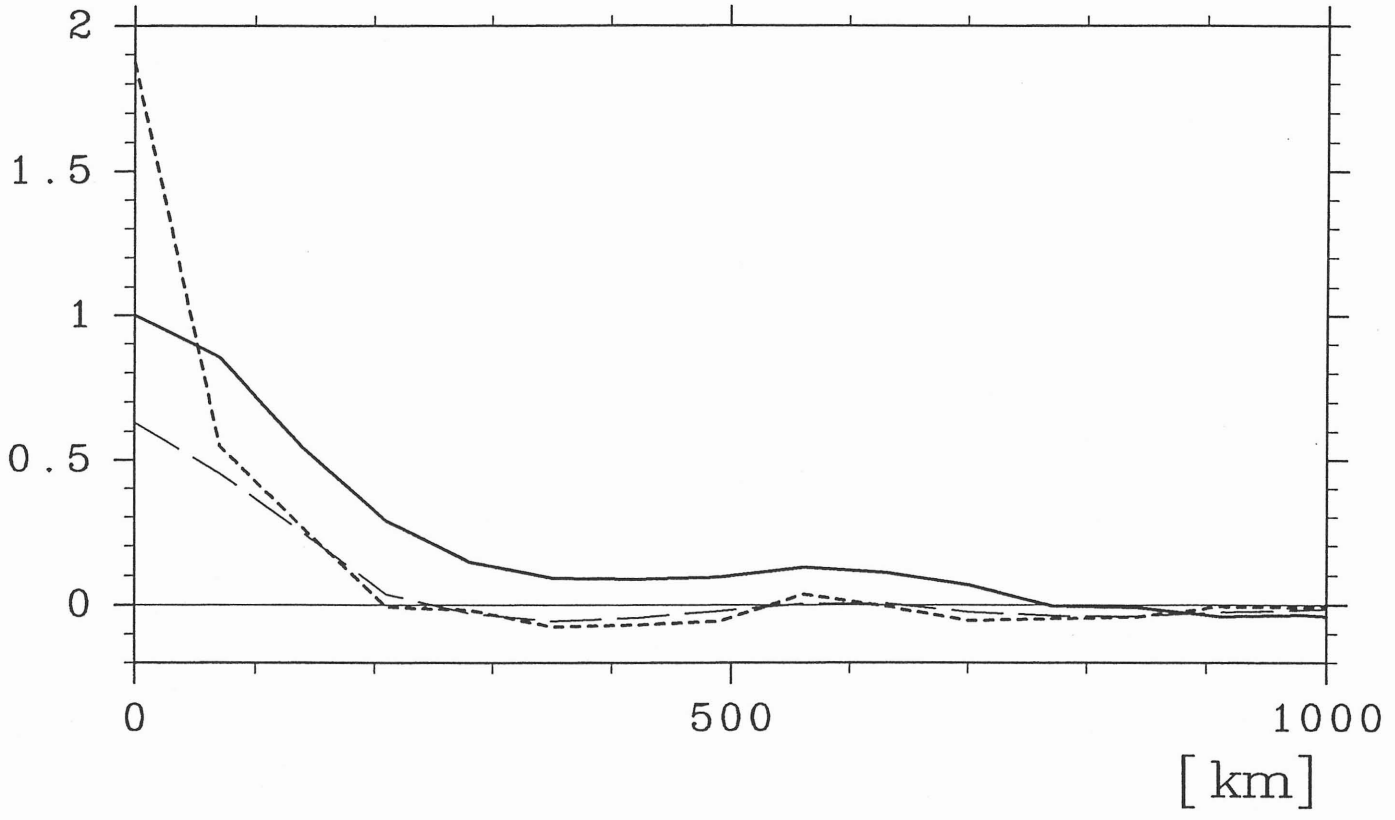

Ichikawa and Imawaki

Fig 13